OCS Study
MMS 2001-056

# Summary of Findings for using High Frequency Radar in Physical Oceanographic and Ecological Studies

## Final Technical Summary

## Final Study Report

**U.S. Department of the Interior**
**Minerals Management Service**
**Pacific OCS Region**

# Summary of Findings for using High Frequency Radar in Physical Oceanographic and Ecological Studies

## Final Technical Summary

## Final Study Report

Authors

**Principal Investigators**
**Libe Washburn**
**Steven Gaines**

Prepared under MMS Cooperative
Agreement No. 14-35-0001-30758
by
Coastal Marine Institute
Marine Science Institute
University of California
Santa Barbara, CA 93106

**U.S. Department of the Interior**
**Minerals Management Service**
**Pacific OCS Region**

**Camarillo**
**March 2001**

## Disclaimer

This report has been reviewed by the Pacific Outer Continental Shelf Region, Minerals Management Service, U.S. Department of the Interior and approved for publication. The opinions, findings, conclusions, or recommendations in this report are those of the authors, and do not necessarily reflect the views and policies of the Minerals Management Service. Mention of trade names or commercial products does not constitute an endorsement or recommendation for use. This report has not been edited for conformity with Minerals Management Service editorial standards.

## Availability of Report

Extra copies of the report may be obtained from:
U.S. Dept. of the Interior
Minerals Management Service
Pacific OCS Region
770 Paseo Camarillo
Camarillo, CA 93010
phone: 805-389-7621

A PDF file of this report is available at:
http://www.coastalresearchcenter.ucsb.edu/CMI/

## Suggested Citation

The suggested citation for this report is:

Libe Washburn and Steven Gaines. Summary of findings for using high frequency radar in physical oceanographic and ecological studies. MMS OCS Study 2001-056. Coastal Research Center, Marine Science Institute, University of California, Santa Barbara, California. MMS Cooperative Agreement Number 14-35-0001-30758. 31 pages.

## Table of Contents


**FINAL TECHNICAL SUMMARY** ..... 1
- Background ..... 1
- Objectives ..... 3
- Description and Results ..... 3
- Significant Conclusions ..... 9
- Study Products ..... 10
- References ..... 12


### List of Figures - Final Technical Summary


Figure 1. Locations of HF radars ..... 4
Figure 2. Spatial pattern of surface currents ..... 5
Figure 3. A. Distribution of dynamic height, 1998
B. Vertical sections of temperature and geostrophic velocity
C. Abundance of 5 fish taxa in the region ..... 6
Figure 4. A. Distribution of dynamic height, 1999
B. Distributions of fish taxa, 1999 ..... 8
Figure 5. Spatial mean currents in the Santa Barbara Channel and Santa Santa Maria Basin, 2000 ..... 9

**FINAL STUDY REPORT** ..... 13
- **Abstract** ..... 13
- **Introduction** ..... 14
- **Methods** ..... 14
- **Results** ..... 17
  - Correlation and radial velocity differences ..... 17
  - Coverage variations ..... 20
  - Spectral analysis ..... 20
  - Bearing offsets ..... 23
- **Discussion** ..... 25
- **Conclusions** ..... 29
- **References** ..... 30


### List of Tables and Figures - Final Study Report


Table 1. HF Radar – mooring comparisons ..... 18
Figure 1. Locations of HF radars ..... 15
Figure 2. Time lines of the moored current time series used for comparison with the HF radar time series ..... 16
Figure 3. Time series of radial currents ..... 19
Figure 4. Time series of coverage showing strong diurnal variations ..... 21
Figure 5. Pairs of power spectra of radial vectors from HF radars and moorings ..... 21
Figure 6. Mean squared coherence spectrum ..... 22
Figure 7. Location of Point Conception radar and mooring ..... 24
Figure 8. Location of Coal Oil Point radar and mooring ..... 24
Figure 9. Bearing offset $\Delta\theta$ versus bearing for all radars with more than one mooring in coverage areas ..... 25
Figure 10. Uniform westward flow parallel to a straight coastline ..... 28

# FINAL TECHNICAL SUMMARY

**STUDY TITLE:** "Application of High Frequency Radar for Surface Current Observations on South-Central California Coast"

**REPORT TITLE:** Summary of findings for using high frequency radar in physical oceanographic and ecological studies

**CONTRACT NUMBER:** 14-35-0001-30758

**SPONSORING OCS REGION:** Pacific

**APPLICABLE PLANNING AREA:** Southern California

**FISCAL YEARS OF PROJECT FUNDING:** FY96, FY97, FY98, FY99

**COMPLETION DATE OF THE REPORT:** 15 March 2001

**COSTS:** FY 96 - $25,000, FY 97 - $91,246, FY 98 - $133,844, FY 99 - $51,727

**CUMULATIVE PROJECT COST:** $301,817

**PROJECT MANAGER:** Russell J. Schmitt

**AFFILIATION:** University of California, Santa Barbara

**ADDRESS:** Coastal Research Center, Marine Science Institute, University of California, Santa Barbara, CA 93106

**PRINCIPAL INVESTIGATORS:** Libe Washburn, Professor, Institute for Computational Earth System Science, Dept. of Geography, University of California, Santa Barbara, CA 93106-3060, email: washburn@icess.ucsb.edu; Steven Gaines, Professor, Dept. of Ecology, Evolution, and Marine Biology, Biology, California, Santa Barbara, CA 93106, email: gaines@lifesci.ucsb.edu

## 1. BACKGROUND:

### 1.1 High frequency radars for ocean current measurement

Since the first observations of the Doppler spectrum of sea echo by [Crombie, 1955], high frequency (HF) radars have become a common technology for studying coastal circulation processes. Despite the increased use of HF radar, several issues remain about their performance in measuring ocean surface currents. For example, the radars' ability to correctly place current vectors on the sea surface, in less-than-ideal deployment situations, remains to be determined. The factors affecting the accuracy and precision of HF radar measurements of surface currents are still not well understood, but in this research we made progress on these issues.

Coastal HF radars for measuring ocean surface currents are divided into two types based on the method used to determine bearing to a sector on the ocean's surface: beam forming radars, such as the Ocean Surface Current Radar (OSCR), and direction finding radars, such as the Coastal Ocean Dynamics Application Radar (CODAR), the system used in our study. Beam forming is accomplished by electronically steering a linear phased array of receive antennas to a sector of ocean surface. Direction finding of the CODAR system uses three receive antenna elements and a variant of the Multiple Signal Classification (MUSIC) algorithm [Schmidt, 1986] to determine bearing. Further discussion of the CODAR system can be found in [Paduan and

Rosenfeld, 1996], [Barrick and Lipa, 1997] and [Barrick and Lipa, 1999]. The beam forming method is discussed by [Graber *et al*., 1997], [Shay *et al*., 1998], and [Vesecky *et al*., 1998].

In 1997 with funding MMS and the W.M. Keck Foundation we began deploying an array of five HF radars along the California coast in conjunction with a large coastal circulation study conducted by the Center for Coastal Studies at the Scripps Institution of Oceanography (CCS/SIO), which included an array of 9 current meter moorings (also MMS funded). We obtained nearly 2 years of overlapping data from the Santa Barbara Channel and Santa Maria Basin that provided the opportunity to investigate the performance of HF radars over a range of conditions and deployment situations. We also used surface circulation data from the radars to address a number of research questions important to coastal marine ecology.

### 1.2 Use of high frequency radar in ecological studies in the Santa Barbara Channel and Santa Maria Basin.

We used a 3-year record of surface currents obtained by an array of HF radars to examine the surface circulation near Pt. Conception, California. We focused on aspects of the circulation important to larval transport and retention. In particular, we examined the role of a persistent cyclonic eddy in the western Santa Barbara Channel. Evidence for larval retention within the eddy came from mid-water trawling surveys for juvenile and late-stage larval fishes in June 1998, 1999, and 2000. The trawling surveys were conducted by Mary M. Nishimoto of the Marine Science Institute at UCSB (MSI/UCSB) and were funded by the Biological Research Division (BRD) at no cost to this project.

During the 1998 survey, a series of midwater trawls were conducted in and around the eddy, finding extremely high concentrations of fishes in its center. During the 1999 and 2000 surveys, high concentrations of fishes were not found and the eddy circulation was not consistently observed. Time series of relative vorticity computed from the HF radar show that the cyclonic circulation was less persistent in 1999 compared with 1998 when it was relatively stable.

Analysis of surface circulation data from 2000 suggests temporal variability similar to 1999 and work on the 2000 biological data is continuing (BRD and UC Sea Grant funded). Patterns of surface currents filtered with a pass band of 7 – 28 days revealed small eddies propagating through the western Santa Barbara Channel which appear to be linked to the stability of the larger cyclonic eddy. Horizontal scales of the eddies are of order 20 km and they propagate westward at about 7 km/day. In 1998 the small eddies began propagating through the region in late June, after the larval development period (approximately March through June). In 1999 the propagation began earlier, in mid-May. Analysis of 2000 data is not yet complete, but the onset of eddy propagation in 2000 appears similar to 1999. We hypothesize that the effectiveness of the eddy as a larval retention mechanism is linked to the stability of the eddy and the onset of the smaller propagating eddies.

We also investigated relationships between settlement patterns of intertidal invertebrates (e.g. crabs, barnacles, limpets, etc.) and evolving patterns of coastal circulation. This analysis is continuing, but some patterns between settlement patterns and coastal circulation have emerged. For example, the typical pattern of offshore surface flow around Pt. Conception is consistent with the fact that the Point is a northern range limit for several species.

## 2.0 OBJECTIVES:

An overall objective our project was to evaluate the performance and feasibility of using high frequency radar systems to measure evolving patterns of surface currents in the waters off the south-central coast (SCC) of California. The study area encompassed the western Santa Barbara Channel and the Santa Maria Basin.

Specific goals were to:

1. To deploy HF radars at three sites along the between Pt. Conception and Pt. Buchon along the south-central coast of California.
2. To compare HF radar-derived surface currents with other, independent measures of surface currents such as *in situ* current meters.
3. To operate the HF radar systems continuously and obtain time series of sufficient length such that the important dynamic processes were resolved spatially and temporally.
4. To compare HF radar-derived surface currents with the spatial and temporal patterns of nearshore plankton distributions, with a specific focus on the movement of larval stages of coastal invertebrates and fishes.

All of these goals were accomplished during the project.

## 3.0 DESCRIPTION AND RESULTS:

### 3.1 HF radar deployments and evaluation.

As discussed above an array of five HF radars were deployed in the Santa Barbara Channel over the course of the project. Three of the radars remain in operation; the other two radars were on loan (at no cost to the project) from NOAA's Environmental Science and Technology Laboratory in Boulder Colorado and had to be returned in February 2001. The coverage area of the HF radar array included eight moorings deployed in the western Santa Barbara Channel and Santa Maria Basin by CCS/SIO (open circles, Figure 1). The CCS/SIO moorings carried vector measuring current meters [Weller and Davis, 1980] at 5 and 45 meters depth providing hourly averages of current velocity. We used the 5 m data for comparison with the surface HF radar data.

An additional mooring was deployed by UCSB investigators near the center of the Santa Barbara Channel from 20 May 1998 to 12 October 1999. The UCSB mooring carried an upward looking 1200 kHz acoustic Doppler current profiler (ADCP; manufactured by R.D. Instruments, San Diego CA) at 15 meters depth. The ADCP measured currents over 0.5 m depth increments (bins) to within 3-4 meters of the sea surface, every 20 minutes. These data were subsequently averaged into 1 hr blocks. Time series from occasional deployments of an electromagnetic current meter (model S4; manufactured by InterOcean, San Diego, CA) at 5 m depth on the UCSB mooring agreed closely with ADCP currents at 5 m. We compared HF radar time series with the time series from the ADCP bin nominally at 4 m depth. This was the shallowest depth consistently free from contamination due to surface reflections.

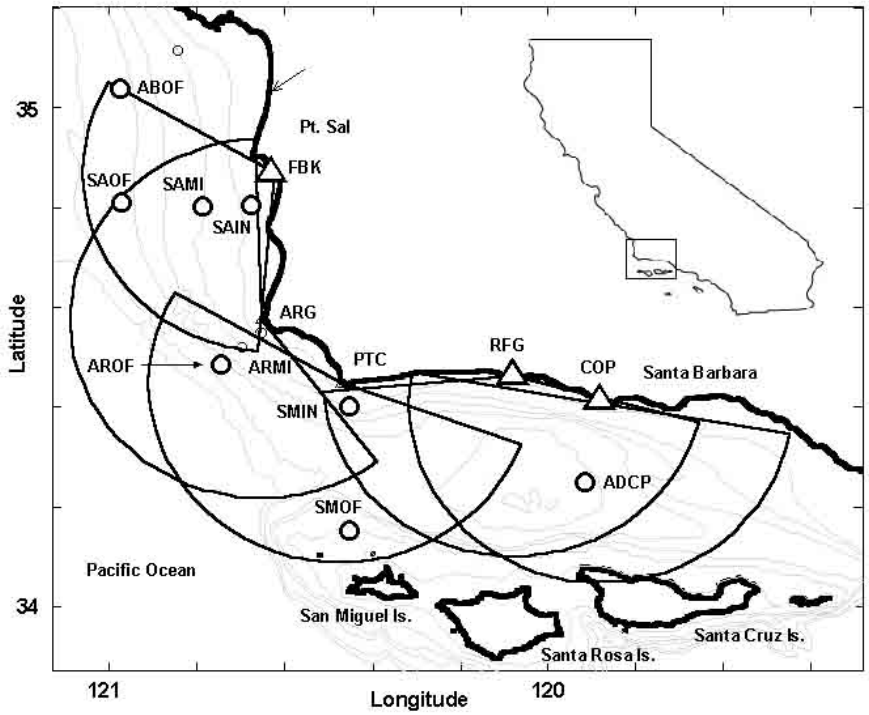


**Figure 1.** Locations of HF radars in the Santa Barbara Channel and Santa Maria Basin are indicated with triangles: FBK is Fallback-22 near Pt. Sal, ARG is Pt. Arguello, PTC is Pt. Conception, RFG is Refugio Beach, and COP is Coal Oil Point. Circular sectors show nominal ranges of 42 km. Circles indicate locations of moored current meters used for comparison with HF radar currents. Naming convention of current meters is discussed in the text. Semi-circles show the extent of HF radar coverage. Bathymetric contours are plotted at 50, 100, 200, 300, 500, and 600 m. The inset shows the study site on the California coast.

We based our study of HF radar performance on comparisons of the radial component of currents observed by the radars with radial components observed by conventional current meters. We focused primarily on the radial current component rather than total velocity vectors because we wanted to evaluate the performance of individual radars. Calculation of total velocity vectors combines measurements of two or more radars and thus, makes evaluation of individual radars more difficult.

To compare radial current vectors (radials) from a HF radar site $V_{HF}$ with those at a particular mooring, we computed the radial component of moored current velocity $V_m$,

$$V_m = \mathbf{V} \bullet \mathbf{i_m} \qquad (1)$$

where $\bullet$ is the dot product, $\mathbf{V}$ is the mooring current velocity, and $\mathbf{i_m}$ is the unit vector pointing from the mooring toward the HF radar site. This procedure was repeated at each mooring for all radars having the mooring within range. A total of 18 paired mooring-HF radar time series were available with maximum record lengths exceeding one year.

To examine performance of individual HF radars, we computed various statistics for each pair of HF radar and mooring time series. The square of the correlation coefficient ($r^2$) was computed between $V_m$ and $V_{HF}$ for the sector containing the mooring, and for sectors surrounding the mooring. Typically, a single HF sector entirely contained the mooring watch circle (50 m to 300 m in radius depending on water depth for the CCS moorings; 750 m for the ADCP mooring). We interpret the value of $r^2$ as an overall measure of similarity between the

time series. Slopes and offsets of regression lines computed between $V_m$ and $V_{HF}$ indicate systematic differences between the time series. Power spectra and squared coherence spectra of $V_m$ and $V_{HF}$ compare the time series across a range of frequencies.

The results of the comparisons between the HF radars and moored current meters are summarized in a paper (attached to this report), "Evaluating radial component current measurements from CODAR high frequency radars and moored *in situ* current meters", that has been submitted for publication [Emery *et al*., 2001].

### 3.2 HF radar in ecological studies of larval transport and advection

In spring 1998, we observed a persistent cyclonic eddy in the western Santa Barbara Channel for several weeks preceding the annual midwater trawling survey conducted by Mary M. Nishimoto of the Marine Science Institute at UCSB (at no cost to this project) in June of that year. The feature was evident in surface current maps generated by HF radar (Figure 2A) and sea surface temperature (SST) imagery from satellite AVHRR (Figure 2B). The persistence of the eddy suggested the possibility that abundance patterns of pelagic juvenile fishes may be related in some way to this flow feature. Accordingly, several midwater trawls were conducted in the eddy and surrounding waters to test this conjecture.

At the beginning of the trawling survey on 2 June 1998 the surface circulation (upper 1 m) in the Channel was strongly cyclonic, as determined by HF radar. The flow in the western Channel was dominated by an eddy centered at 120.1 W, 34.3 N with a diameter of about 30 km and maximum azimuthal currents of about 0.4 m $s^{-1}$ (Figure 2A). The rotation of the eddy, quantified by its relative vorticity, ranged from 0.2 $f$ (rotation period of ~ 9 days) on the periphery to about 0.7 $f$ (rotation period of ~3 days) in the center, where $f$ is the Coriolis parameter. Strong rotary flow in the eddy was also indicated by alternating warm and cool streaks wrapped around the eddy as revealed by sea surface temperature (SST) imagery (Figure 2B). Time series of surface currents obtained from the HF radars showed that the eddy persisted throughout the juvenile fish survey.

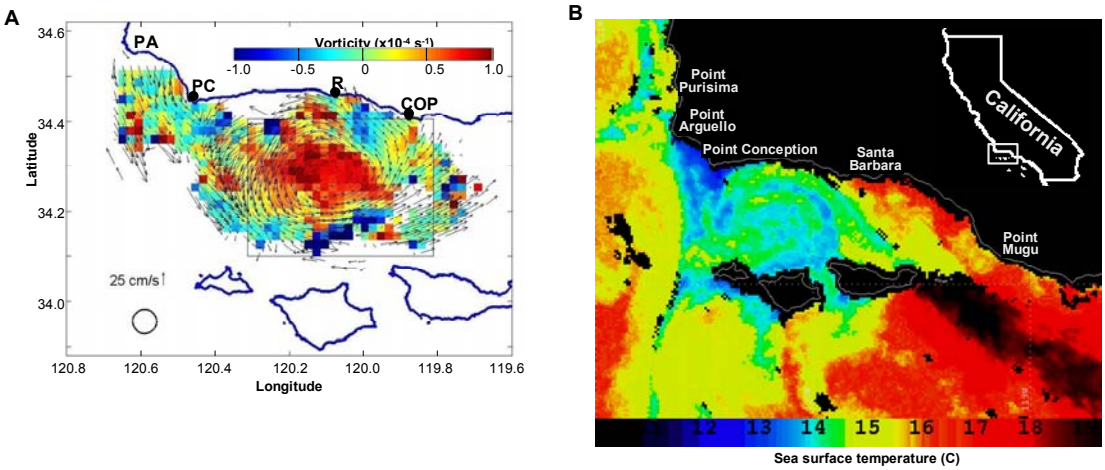


**Figure 2.** **(A)** Spatial pattern of surface currents at 1900 GMT on 2 June 1998 showing a strong cyclonic eddy in the western Santa Barbara Channel. Surface currents were mapped with HF radars at Coal Oil Point (COP), Refugio (R), and Point Conception (PC). Scale for current speed is at lower left. Circle (radius=3 km) at lower left is the area over which current vectors are averaged. **(B)** The cyclonic eddy is visualized by curving temperatures features wrapping around the eddy in the satellite sea surface temperature image at 0152 GMT on 3 June 1998.

The eddy circulation was not merely a surface flow, but extended to at least 200 m depth. The spatial pattern of dynamic height ϕ, determined from CTD casts during the trawling survey, had a minimum in the core of the eddy, consistent with the strong cyclonic circulation revealed by the HF radars (Figure 3A). Assuming a level of no motion at 200 dbar (~200 m depth), the sea surface (0 dbar) was lower in the center by about 0.05 m compared with surrounding waters. We defined the eddy center by $\phi \leq 0.32$ m.

Isolines of potential temperature T along an east-west section across the eddy showed the effects of the earth's rotation by rising sharply in the eddy center (Figure 3B). The 10°C isotherm rose about 80 m in the center; similar deflections were also apparent for salinity and density. Horizontal density gradients in the eddy supported vertical shear in horizontal currents; the speed of these geostrophic currents changes by about 0.2 m $s^{-1}$ over the 200 m measurement interval. Currents across the section show southward flow at depth west of the center and northward flow to the east, consistent with deep cyclonic flow (Figure 3B). Deflections of the deepest isolines indicated the cyclonic circulation of the eddy extended below 200 m.

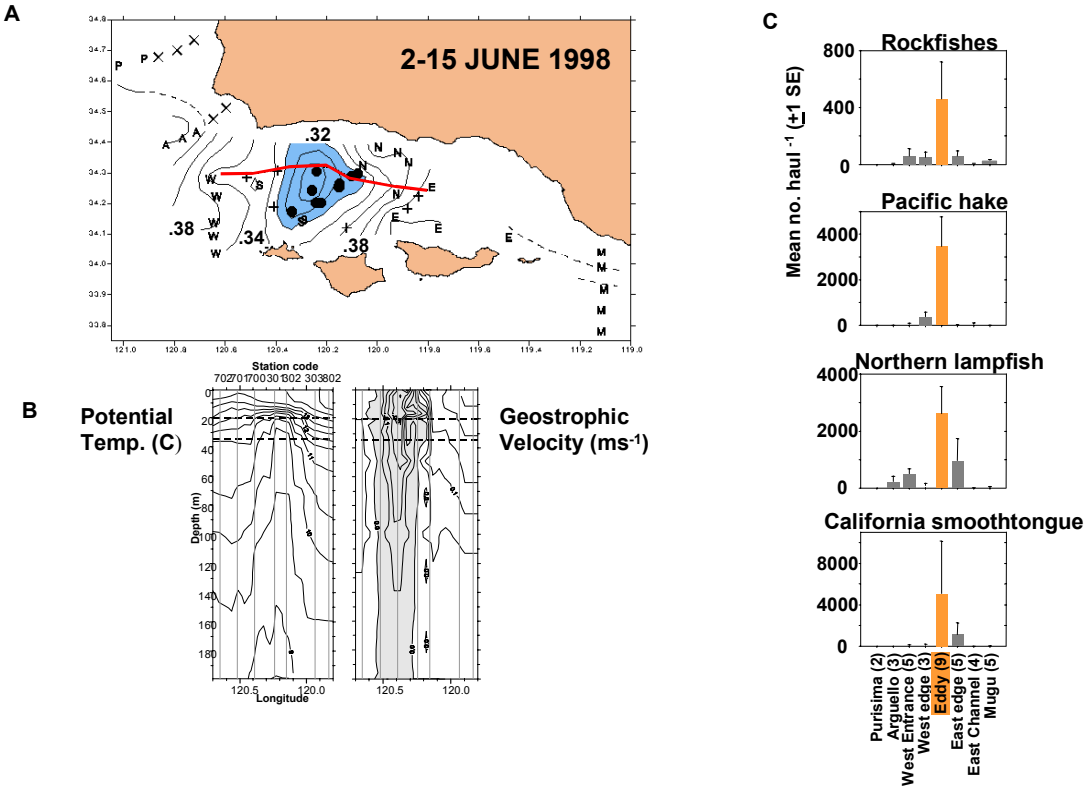


**Figure 3.** **(A)** Distribution of dynamic height in the western Santa Barbara Channel during trawling surveys in 1998. **(B)** Vertical sections of temperature and geostrophic velocity along bold line in panel A. **(C)** Abundance of 5 fish taxa in the region. High concentrations of fishes were found in the center of the eddy. In panel A, P indicates Purisima, A is Arguello, W. is west Channel, + signs are east and west edges, E is east Channel, N is north Channel, and M is Mugu..

During the two weeks of sampling, 2-15 June, net hauls were conducted in the eddy and surrounding waters to look for possible influences on juvenile fish abundance. In post-cruise analysis, hauls were grouped into seven geographic areas, including the eddy center that was defined by $\phi < 0.32$ m. The abundance of each of the five dominant taxa was greatest in the eddy center (Figure3C). The fishes were patchily distributed, and occasional large catches

occurred at the southwest and northeast edges of the eddy and at the west entrance of the Channel. Catches of rockfishes (*Sebastes* spp.) and Pacific hake (*Merluccius productus*), two abundant taxa represented by late-stage larvae and pelagic juveniles, were 39 to $1.1 \times 10^4$ haul$^{-1}$ in the center compared with north of the Channel and in the east Channel where catches were typically less than 100 haul$^{-1}$. Mesopelagic fishes California smoothtongue (*Leuroglossus stilbius*), northern lampfish (*Stenobrachius leucopsarus*), and Mexican lampfish (*Triphoturus mexicanus*), represented by juveniles and adults, exhibited similarly high abundance and possible entrainment in the eddy center.

The striking observation motivated us to repeat the survey in 1999 and 2000. Results from the 1999 and 2000 surveys were characterized by very different larger-than-channel scale and mesoscale oceanographic conditions and catch distributions. Physical conditions in the Channel in June 1999 were much different than June 1998; perhaps the biggest difference was the stronger winds in 1999 associated with La Niña conditions.

Circulation in the Channel was highly variable in 1999 compared to the stable cyclonic eddy flow pattern observed in 1998. In 1999, temperature-salinity distributions changed rapidly as indicated by repeated sampling in the western Channel (Figure 4A). During the first leg of sampling, 6-21 June 1999, dynamic height was low in the Channel north of the San Miguel-Santa Rosa Islands passage and corresponded with a cyclonic eddy feature observed by HF radar at the time of sampling. The gradient in dynamic height across the feature was similar to that in 1998. Dynamic height at 5 m depth (5 dbar) assuming a level of no motion at 200dbar was lower in the center by about 0.05 m compared with surrounding waters. We defined the center as $\phi \leq$ 0.34 m. Re-sampling during 24 June-1 July (leg 2) revealed that dynamic height increased in that area, and a low dynamic height feature with $\phi \leq 0.34$ m as its center was observed west of the Channel entrance (Figure 4A). The area to the west of the Channel was beyond HF radar coverage and was not sampled during leg 1.

The flow field in the few months preceding and during the 1999 survey was characterized by propagating trains of eddies with alternating cyclones (rotating clockwise) and anti-cyclones (rotating counterclockwise) along with increased flow from the east entrance through the Channel. These eddies were discussed in presentations at the 2000 AGU meeting in San Francisco by Beckenbach and Washburn and by Washburn *et al*.). Coherence of the spatial distributions of the dynamic height from legs 1 and 2 and HF radar data suggested that we sampled twice an eddy that propagated westward from within the Channel to the western entrance. The importance of these eddies is one of the focuses of our ongoing research.

Abundance of the dominant fish taxa and their spatial distributions differed substantially between 1998 and 1999. Catch abundance in 1999 was lower by an order of magnitude compared to 1998). The five taxa comprised 98% and 96% of the mean total catch in 1998 and 1999, respectively. Rockfishes were the fifth most abundant taxa in 1998. In 1999, sanddabs (*Citharichthys* spp.) and northern anchovy (*Engraulis mordax*) were slightly more abundant than rockfishes.

We grouped the 1999 trawling stations by $\phi$ and geographic area as we did with the 1998 samples. Furthermore, we divided the 1999 samples into two sampling periods (Figure 4B). In contrast to 1998, late-larval stage and pelagic juvenile rockfishes and Pacific hake were more

abundant north of the Channel off Pt. Purisima than in the Channel, and their distributions did not show a relationship with dynamic height features in 1999. Northern lampfish and California smoothtongue, both represented by juvenile and adults, were more abundant in the western Channel during the first sampling period when it was occupied by a cyclonic eddy with a center of low dynamic height ("Low_leg 1") than during the second sampling leg when the area is characterized by high dynamic height ("Chan_leg 2"). No consistent relationship between dynamic height areas and the spatial distribution of the dominant taxa in the Channel was observed in 1999.

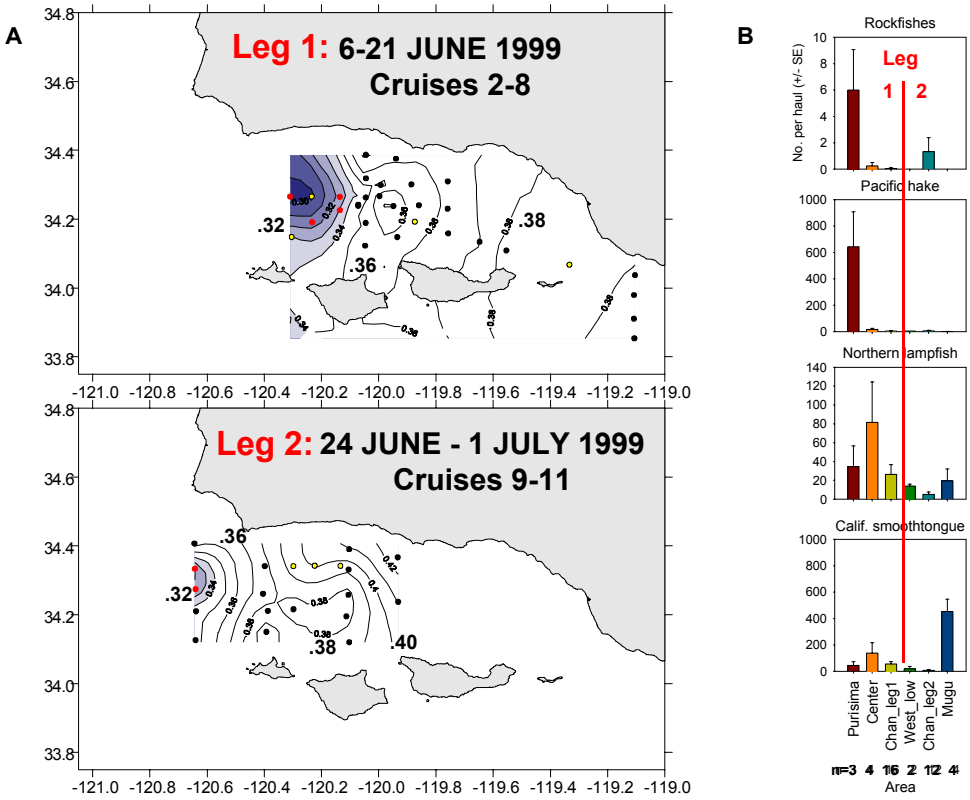


**Figure 4.** **(A)** Distribution of dynamic height in the western Santa Barbara Channel during trawling surveys of 1999. **(B)** Distributions of fish taxa during 1999 surveys.

Flows in the western Santa Barbara Channel and Santa Maria Basis were also compared with recruitment patterns of several invertebrate species. Recruitment was measured as part of the Partnership for Interdisciplinary Studies of the Coastal Ocean (PISCO) (at no cost to this project) along several sites on the south-central California coast including three in the HF radar coverage area (green squares, Figure 5). A typical regional flow pattern from summer 2000 shows strong equatorward and offshore flows outside the Channel consistent with prevailing upwelling favorable winds. The upwelling center around Points Conception and Arguello had mean offshore flows of about 10 cm/s when averaged over a six week period. The along shore distribution of settlement of 13 species showed a minimum at the recruitment site within this upwelling center (red arrow and bars in inset diagram of Figure 5). This suggests a strong link between settlement patterns of inter-tidal invertebrates and persistent coastal circulation features such as this upwelling center. We are continuing our investigation of links between settlement patterns and coastal circulation as part of PISCO.

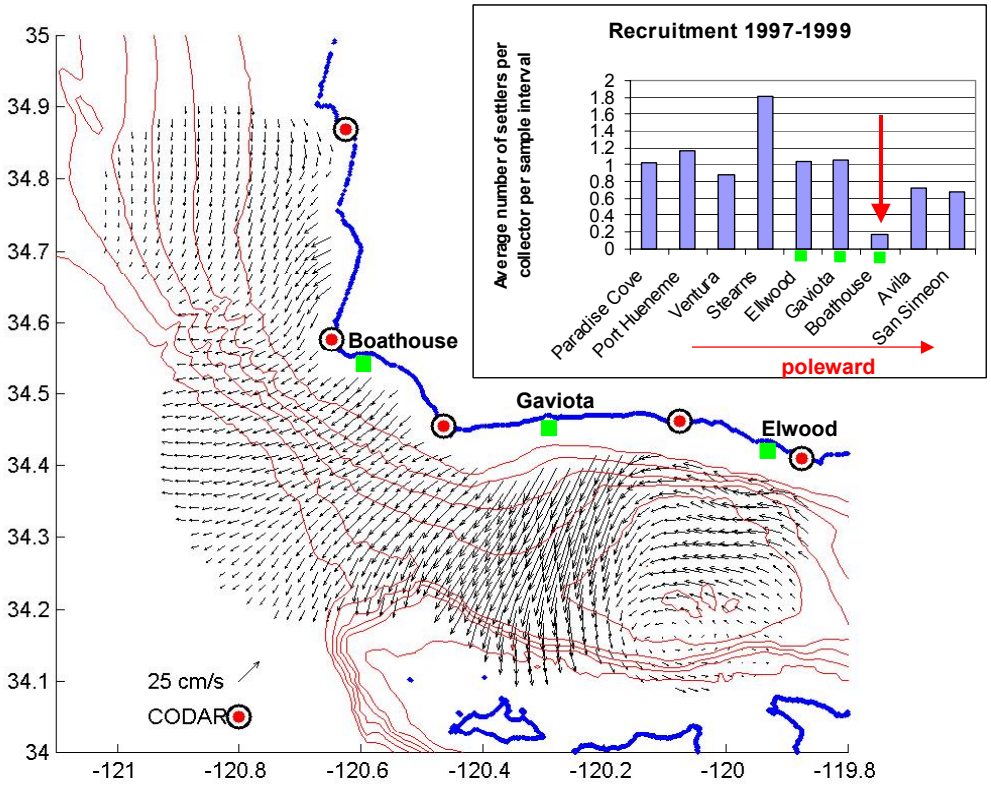


**Figure 5.** Spatial mean currents in the Santa Barbara Channel and Santa Maria Basin during 6 June – 26 July, 2000. Inset shows inter-tidal recruitment at several sites. Squares show recruitment sites within radar coverage area. Arrow in inset indicates low settlement in the upwelling center between Points Conception and Arguello. Black circles and dots indicate HF radar sites.

## 4.0 SIGNIFICANT CONCLUSIONS:

### 4.1 Radar performance

Our investigation of the performance of HF radars for measuring surface currents supports the following conclusions:

1. Radial currents obtained from the radars were significantly correlated with radial currents obtained from the moored current meters with $r^2$ in the range 0.39-0.77. Root-mean-square (rms) radial speed differences ranged from 7-19 cm $s^{-1}$. A weak trend of increasing rms differences was found with increasing range.
2. Significant coherence was found between current meter and radar-derived time series for frequencies below 2.2 cpd (11 hour period and longer). Power spectra showed similar magnitudes and slopes for frequencies below 2.2 cpd.
3. A pointing error $\Delta\theta$ ranging from $-16^o$ to$19^o$ was found for some of the radar sites where positive values indicate a clockwise error. $\Delta\theta$ for a given radar was not constant, but varied with bearing. We speculate that $\Delta\theta$ resulted from distortions of the receive antenna patterns in the near field.

4. We used a simple model of $\Delta\theta$ versus bearing based on our observations to simulate errors in total velocity vectors computed from two radars. Using a uniform flow parallel to shore, $\Delta\theta$ produced speed errors of up 15% and direction errors up to $9^o$ in total velocity vectors We are working with colleagues at CODAR Ocean Sensors, Oregon State University, and the Naval Postgraduate School to correct these errors in processing algorithms for HF radar data.

### 4.2 Application of HF radar to coastal circulation and marine ecology

1. Persistent cyclonic circulation is a dominant flow pattern in the western Santa Barbara Channel consistent with results of [Dever *et al.*, 1998; Harms and Winant, 1998; Winant *et al.*, 1999].
2. Propagating trains of eddies occur in the western Santa Barbara Channel. The eddies have horizontal scales of order 15 km, current speeds of 0.1-0.2 m/s, and alternating relative vorticity of magnitudes comparable to the vertical component of the earth's rotation rate. They propagate westward at ~7 km/day. Their high relative vorticity indicates that the eddies are not in simple geostrophic balance, but rotate rapidly enough to produce significant centripetal acceleration. We use the term "eddy" to describe the features, but they may be some type of wave such as a topographic Rossby wave.
3. Animations of HF radar data show that surface currents respond rapidly to changes in local wind velocity, especially in the Santa Maria Basin.
4. Very high concentrations of juvenile and late stage larval occur in the western Santa Barbara Channel under conditions of stable cyclonic flow
5. Propagating eddies can prevent establishment of stable circulation patterns that might otherwise retain larvae.
6. Coastal circulation features such as the upwelling center between Points Conception and Arguello limit settlement in the region due to strong persistent offshore advection driven by upwelling-favorable winds.

## 5.0 STUDY PRODUCTS:

### Publications:

Emery, B.M., L. Washburn, and J. Harlan, Evaluating CODAR high frequency radars for measuring surface currents: observations in the Santa Barbara Channel, *Journal of Atmospheric and Oceanic Technology (manuscript submitted)*, 2001.

Beckenbach, E.H. and L. Washburn, Propagating eddies in the Santa Barbara Channel, in preparation.

Washburn, L. and S. Gaines. Summary of findings for using high frequency radar in physical oceanographic and ecological studies. MMS OCS Study 2001-056. Coastal Research Center, Marine Science Institute, University of California, Santa Barbara, California. MMS Cooperative Agreement Number 14-35-0001-30758. 32 pages.

**Presentations:**

2000 Surface circulation near Pt. Conception, California: A mechanism for larval retention?, Washburn, L., M.M. Nishimoto, E.H. Beckenbach, and B.M. Emery, Fall Meeting, American Geophysical Union, San Francisco, 15-19 September.

2000 Observations of propagating eddies in the Santa Barbara Channel, Beckenbach, E.H., L. Washburn, D. Salazar, and B.M. Emery, Fall Meeting, American Geophysical Union, San Francisco, 15-19 September.

2000 Time series mapping of currents in the coastal ocean, Kosro, P.M., J.D. Paduan, and L. Washburn, Fall Meeting, American Geophysical Union, San Francisco, 15-19 September.

2001 Surface circulation on the South-central coast: Mechanisms for larval transport and retention, seminar in the Dept. of Atmospheric Science, UCLA, 24 January.

2001 Variability in mesoscale oceanographic processes corresponds to variability in the distribution and abundance of rockfish (*Sebastes* spp.) juveniles, Schroeder, D M , M.M. Nishimoto, and L. Washburn, American Society of Limnology and Oceanography, Albuquerque2001, Albuquerque, NM, 12-16 February.

2001 The physical environment of the Santa Barbara Channel, seminar presented to volunteers of the Channel Islands National Marine Sanctuary", Chase Palm Park, 1 March.

## 6.0 REFERENCES:

Barrick, D.E., and B.J. Lipa, Evolution of bearing determination in HF current mapping radars, *Oceanography*, *10* (2), 72-75, 1997.

Barrick, D.E., and B.J. Lipa, Using antenna patterns to improve the quality of SeaSonde HF radar surface current maps, *IEEE 6th Working Conference on Current Measurement*, 1999.

Crombie, D.D., Doppler Spectrum of Sea Echo at 13.56 Mc/s, *Nature*, *175*, 681-682, 1955.

Dever, E.P., M.C. Henderschott, and C.D. Winant, Statistical Aspects of surface drifter observations of circulation in the Santa Barbara Channel, *Journal of Geophysical Research*, *103* (C11), 24,781-24,797, 1998.

Emery, B.M., L. Washburn, and J. Harlan, Evaluating CODAR high frequency radars for measuring surface currents: observations in the Santa Barbara Channel, *in preparation for Journal of Atmospheric and Oceanic Technology (manuscript available)*, 2001.

Graber, H.C., B.K. Haus, R.D. Chapman, and L.K. Shay, HF radar comparison with moored estimates of current speed and direction: Expected differences and implications, *Journal of Geophysical Research*, *102* (C8), 18,749-18,766, 1997.

Harms, S., and C.D. Winant, Characteristic patterns of the circulation in the Santa Barbara Channel, *Journal of Geophysical Research*, *103* (C2), 3041-3065, 1998.

Paduan, J.D., and L.K. Rosenfeld, Remotely sensed surface currents in Monterey Bay from shore-based HF radar (Coastal Ocean Dynamics Application Radar), *Journal of Geophysical Research*, *101* (C9), 20,669-20,686, 1996.

Schmidt, R.O., Multiple Emitter Location and Signal Parameter Estimation, *IEEE Transactions on antennas and propagation*, *AP-34* (3), 276-280, 1986.

Shay, L.K., S.J. Lentz, H.C. Graber, and B.K. Haus, Current structure variations detected by high-frequency radar and vector-measuring current meters, *Journal of Atmospheric and Oceanic Technology*, *15*, 237-256, 1998.

Vesecky, J., C. Teague, D. Fernandez, J. Paduan, J. Daida, R. Onstott, K. Laws, and P. Hansen, Coastal Currents with HF radar, *Backscatter*, *13*, 12-20, 1998.

Weller, R.A., and R.E. Davis, A vector measuring current meter, *Deep-Sea Research*, *27*, 565-582, 1980.

Winant, C.D., D.J. Alden, E.P. Dever, K.A. Edwards, and M.C. Henderschott, Near-surface trajectories off central and southern California, *Journal of Geophysical Research*, **104** (C7): 15,713-15,726, 1999.

# FINAL STUDY REPORT

## Evaluating radial component current measurements from CODAR high frequency radars and moored in situ current meters

Brian M. Emery[1], Libe Washburn[2], and Jack A. Harlan[3]

[1]Institute for Computational Earth System Science, University of California, Santa Barbara, 93106-3060; [2]Department of Geography, University of California, Santa Barbara, 93106-4060; [3]NOAA Environmental Technology Laboratory, Boulder, Colorado

### Abstract

The performance of a network of five CODAR (Coastal Ocean Dynamics Application Radar) high frequency (HF) radars is described based on comparisons with an array of nine moorings in the Santa Barbara Channel and Santa Maria Basin deployed between June 1997 and November 1999. Eight of the moorings carried vector measuring current meters (VMCM's), the ninth an upward-looking acoustic Doppler current profiler (ADCP). Coverage areas of the HF radars and moorings included diverse flow and sea state regimes. Measurement depths were ~1 m for the HF radars, 5 m for the VMCM's, and 3.2 m for the nearest ADCP bin to the surface. Comparison of radial components of near-surface currents from 18 HF radar-mooring pairs yielded root mean square (rms) speed differences of 7-19 cm $s^{-1}$. The radial components were significantly correlated with $r^2$ in the range 0.39-0.77. Other studies based on radar-mooring comparisons have found similar rms speed differences and $r^2$ based on total velocity vectors. Spectral analysis showed significant coherence for frequencies below 2.3 cycles $day^{-1}$ (periods longer than 11 hr). At higher frequencies no significant coherence was found. Comparisons revealed bearing errors in locating radial currents on the sea surface by some of the HF radars. These were typically 5-10° with a maximum error of 19º. The effects of bearing errors on total velocity vector estimates were evaluated using a simple flow field and measured bearing errors, showing up to 15% differences in computed flow speeds, and up to ~9º differences in flow directions.

### 1. Introduction

Since the first observations of the Doppler spectrum of sea echo by (Crombie 1955), high frequency (HF) radars have become a common technology for studying coastal circulation processes. Despite its increased use, several issues remain about the performance of HF radar for measuring surface currents. For example, the radars ability to determine bearing to radial current vectors on the sea surface in less-than-ideal deployment situations remains to be quantified. In 1997, we began deploying an array of five HF radars along the California coast in conjunction with a large coastal circulation study conducted by the Center for Coastal Studies at the Scripps Institution of Oceanography (CCS/SIO), which included an array of 9 current meter moorings. Nearly 2 years of overlapping data from the moorings and the radars provides the opportunity to evaluate some of the performance characteristics of the HF radars.

Coastal HF radars for measuring surface currents are divided into two types based on the method used to determine bearing to a sector on the ocean's surface: beam forming radars, such

as the Ocean Surface Current Radar (OSCR), and direction finding radars, such as the Coastal Ocean Dynamics Application Radar (CODAR), the system used in this study. Beam forming in the OSCR system is accomplished by electronically steering a linear phased array of receive antennas to a sector of ocean surface (Kraus 1988). Direction finding of the CODAR system uses three receive antenna elements and a variant of the Multiple Signal Classification (MUSIC) algorithm (Schmidt 1986) to determine bearing. Further discussion of the CODAR system can be found in (Paduan and Rosenfeld 1996), (Barrick and Lipa 1997), and (Barrick and Lipa 1999). The beam forming method is discussed by (Graber *et al.* 1997), (Shay *et al.* 1998), and (Vesecky *et al.* 1998). We limit our discussion to HF radars that use ground wave propagation, via conductance along the ocean surface, rather than skywave or ionospheric propagation (e.g., Georges 1980).

Despite different bearing determination methods used by the OSCR and CODAR radars, underlying physics produce operational similarities between the systems. Thus, some results obtained by comparisons between *in situ* current meters and either type of radar may apply to both systems. In particular (Graber *et al.* 1997) and (Shay *et al.* 1998) used an OSCR system to identify numerous sources of error common to both. These include differences in spatial and temporal sampling, horizontal variability of currents, near-surface vertical shear, Stokes drift, Ekman flow, and measurement errors due to current meters. Other comparisons have examined many of these factors including (Chapman *et al*. 1997), (Chapman and Graber 1997), (Shay *et al.* 1998), (Paduan and Rosenfeld 1996), and (Kosro *et al.* 1997).

With few exceptions (e.g. Melton 1995 and Harlan *et al*. 2000), previous studies of HF radar performance compared *total* velocity vectors from *in situ* current meters and HF radars. Because total velocity vectors are computed from radial components from two (or more) HF radars, errors from individual radars are combined. Errors in total vectors also result from geometric dilution of precision (Chapman and Graber 1997). We compared *radial* components with moored current meters to evaluate performance of individual radars.

The rest of this report is organized as follows: In section 2 we discuss the radar and mooring deployments and data analysis procedures; results of comparisons of radial currents from the radars and current meters are presented in section 3; section 4 is a discussion; and conclusions are in section 5.

## 2. Methods

In 1997 we began deploying HF radars along the western Santa Barbara Channel and south-central California coasts (Figure 1). The first was installed at Coal Oil Point (COP) in June 1997, followed by Pt. Conception (FTC) in August 1997, then Refugio (RFG) in October 1997. The fourth and fifth were installed in November 1998 at Pt. Arguello (ARG) and Faliback 22 (FBK) near Pt. Sal. Each site consists of a transmit antenna, a receive antenna, radar electronics, and a computer for control and data logging. The radar electronics and computers are either housed in buildings (FTC and COP), or in weather proof enclosures. Antennas were placed as close to the ocean as possible to minimize signal attenuation by propagation over land.

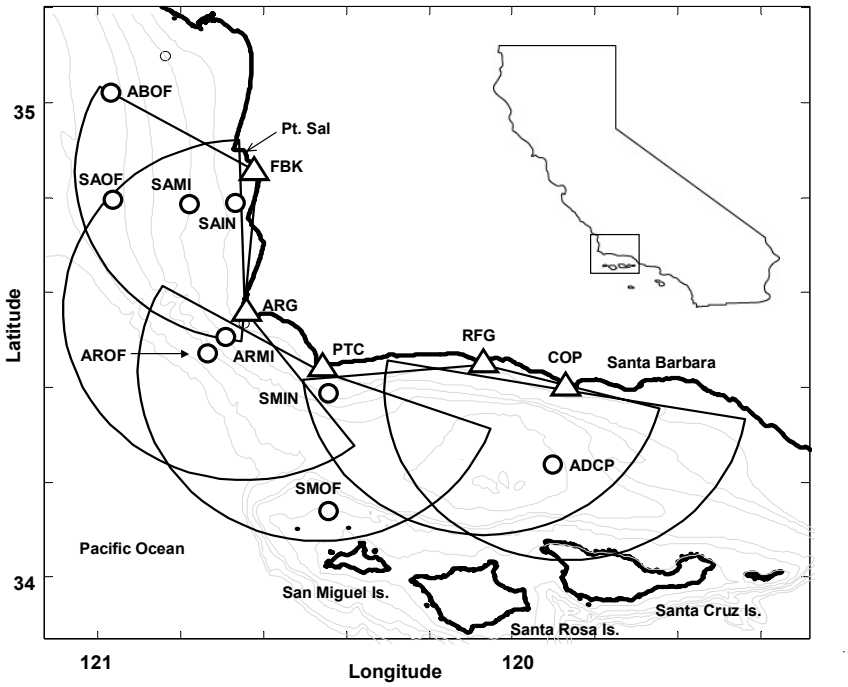


**Figure 1.** The Santa Barbara Channel and Santa Maria Basin. Locations of HF radars are indicated with triangles: Fallback-22 near Point Sal (FBK), Point Arguello (ARG), Point Conception (PTC), Refugio Beach (REG), and Coal Oil Point (COP). Circular sectors show nominal radar ranges of 42 km. Circles indicate locations of moored current meters used for comparison with HF radar currents. Naming convention of current meters is discussed in text. The inset shows the study site relative to the California coast.

Each radar transmits at a different frequency in the range 12.2 - 13.6 megahertz. Following the Bragg principle, transmitted signals are backscattered from ocean surface waves with wavelengths of ~12 m, half the ~24 m transmitted wavelength. In the absence of any current, the backscattered radar signals are Doppler shifted by an amount proportional to the intrinsic phase velocity of the 12 m ocean waves, determined from the deep-water wave dispersion relation. Ocean current velocity is determined from the difference between the measured and intrinsic phase velocities. Based on the transmit frequency, this measurement corresponds to the velocity of the upper ~1 m of the ocean surface (Stewart and Joy 1974). Range to a sector of ocean surface is determined using frequency modulation, which divides the coverage area into concentric circular arcs called range cells. As implemented by CODAR Ocean Sensors, Ltd., the MUSIC algorithm divides these range cells into azimuthal sectors of ocean surface and estimates the bearing to each sector (Barrick and Lipa 1997, Laws *et al.* 2000). Radial currents are smoothed in bearing (azimuth measured clockwise from north) at 2° intervals with a 10° running average. For our study each sector spanned 1.5 km in range and 5° in bearing. The sector areas (depicted graphically in Figure 6a) varied linearly from 0.2 $km^2$ to 5.5 $km^2$ as range varied from 1.5 to 42 km. Radial current estimates were computed every 10 minutes and these were averaged to produce an hourly radial vector for each sector, although gaps typically occurred in the time series.

The coverage area of the HF radar array included eight moorings deployed in the western Santa Barbara Channel and Santa Maria Basin (open circles, Figure 1) from 1993 to 1999 by CCS/SIO. Time lines of mooring and HF radar data used for comparison are shown in Figure 2. The CCS/SIO moorings carried vector measuring current meters (Weller and Davis 1980) at 5

and 45 meters depth providing hourly averages of current velocity. We use the 5 m data for comparison with the surface HF radar data. As explained by (Harms and Winant 1998), the CCS/SIO moorings were named according to location and position on the continental shelf (Figure 1). The first two letters indicate mooring lines: AB for Avila Beach, SA for Pt. Sal, AR for Pt. Arguello, and SM for San Miguel Island. The second two letters indicate position within a mooring line: OF is offshore, MI is mid-shelf, and IN is inshore. For example, SAIN identifies the inshore mooring at Pt. Sal.

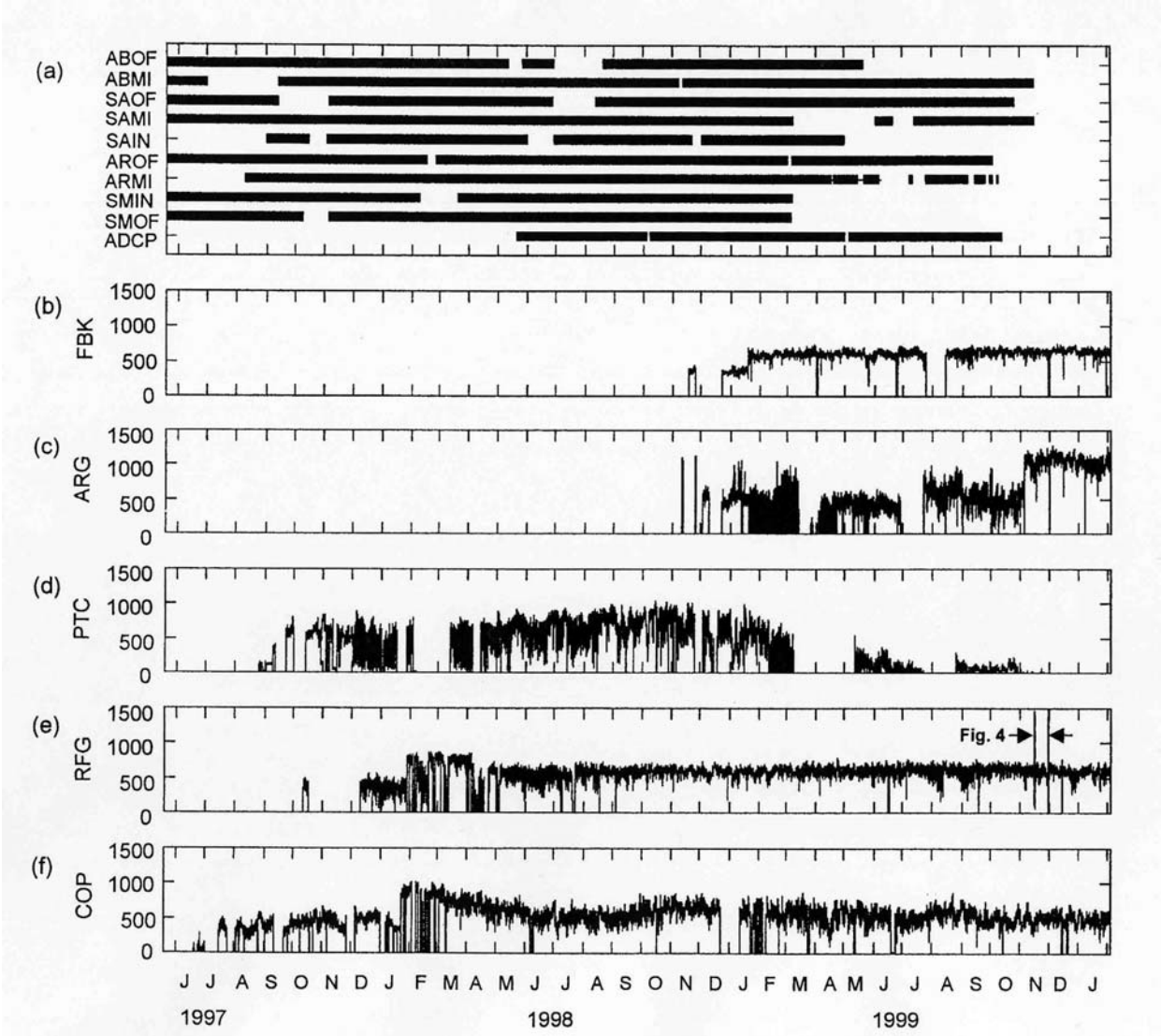


**Figure 2. (a)** Time lines of the moored current time series used for comparison with the HF radar time series. **(b-f)** Time series of coverage defined as the number of sectors returning data each hour for the five HF radars. Vertical bars toward the end of the RFG time series denote the two week segment of Figure 4.

An additional mooring, designated ADCP in Figures 1 and 2, was deployed by UCSB investigators near the center of the Santa Barbara Channel from 20 May 1998 to 12 October 1999. The UCSB mooring carried an upward looking 1200 kHz acoustic Doppler current profiler (ADOP; manufactured by R.D. Instruments, San Diego CA) at 15 meters depth. The ADCP measured currents over 0.5 m depth increments (bins) to within 3-4 meters of the sea surface, every 20 minutes. These data were subsequently averaged into 1 hr blocks. Time series from

occasional deployments of an electromagnetic current meter (model S4; manufactured by InterOcean, San Diego, CA) at 5 m depth on the UCSB mooring agreed closely with ADCP currents at 5 m. We compared HF radar time series with the time series from the ADCP bin nominally at 3.2 m depth. This was the shallowest depth consistently free from contamination due to surface reflections.

To compare radial current vectors $V_{HF}$ (radials) from a radar site with those at a particular mooring, we computed the radial component of moored current velocity $V_m$,

$$V_m = \mathbf{V} \cdot \mathbf{i_m} \qquad (1)$$

where • is the dot product, **V** is the mooring current velocity, and $\mathbf{i_m}$ is the unit vector pointing from the mooring toward the HF radar site. This procedure was repeated at each mooring for all radars having the mooring within range. A total of 18 paired mooring-HF radar time series were available with maximum record lengths exceeding one year (Figure 2 and Table 1).

To examine performance of individual HF radars, we computed various statistics for each pair of HF radar and mooring time series. The square of the correlation coefficient ($r^2$) was computed between $V_m$ and $V_{HF}$ for the sector containing the mooring, and for sectors surrounding the mooring. Typically, a single radar sector entirely contained the mooring watch circle *(*50 m to 300 m in radius depending on water depth for the GCS/SIO moorings; 750 m for the ADCP mooring). We interpret $r^2$ as an overall measure of similarity between the time series. Rms differences were computed with means removed, with the difference in the means reported as the bias. Biases, along with slopes and offsets of regression lines computed between $V_m$ and $V_{HF}$ indicate systematic differences between the time series. Power spectra and squared coherence spectra of $V_m$ and $V_{HF}$ compare the time series across a range of frequencies.

## 3. Results

### 3.1 Correlation and radial velocity differences

Time series of $V_{HF}$ and $V_m$ typically showed strong tidal variations as in the 2-week example from FBK-SAMI (Figure 3a). The time series were clearly similar and exhibited significant correlation for this short interval ($r^2$ =0.81, N=314; Figure 3b). Table 1 summarizes the statistical comparisons between $V_{HF}$ and $V_m$ for all HF radar-mooring pairs over much longer time scales. Variations in the comparison periods (columns 3 and 4) mainly resulted from changing coverage for some of the radars due to hardware problems. Values of $r^2$ fell in the range 0.39-0.77 (column 8), and root-mean-square (rms) speed difference ranged from 7-19 cm $s^{-1}$ (column 11). Biases (column 12) were typically less than 2 cm $s^{-1}$, with a maximum of 6 cm $s^{-1}$. Slopes m of regression lines, defined such that $V_{HF} = V_m \bullet m + b$, were in the range 0.31-0.88 with intercepts b in the range 4.5-8.4 cm $s^{-1}$ (columns 13 and 14).

**Table 1. HF radar – mooring comparisons**. Summary of comparison statistics for 18 HF radar - moored current meter pairs. HF site name and mooring name abbreviations are described in the text. [1] HF radar - mooring pairs used in the calculation of the Mean squared coherence spectrum $\overline{\gamma^2}$ (Figure 6).

| 1 HF site | 2 Mooring | 3 Start date | 4 End date | 5 Data Points (hourly) | 6 Bearing (deg) | 7 Range (km) | 8 $r^2$ | 9 $\Delta\theta$ (deg) | 10 $\lvert\Delta\theta\rvert$ (deg) | 11 RMS (cm/s) | 12 Bias (cm/s) | 13 HF = VMCM*m+b m | 14 b |
|---|---|---|---|---|---|---|---|---|---|---|---|---|---|
| FBK | ABOF | 1-Feb-99 | 14-Nov-99 | 125 | 299 | 36.7 | 0.59 | 16 | 16 | 11 | -2 | 0.634 | 4.3 |
| FBK | SAOF[1] | 1-Feb-99 | 15-Nov-99 | 5227 | 258 | 32.6 | 0.59 | -8 | 8 | 11 | -1 | 0.761 | 0.3 |
| FBK | SAMI[1] | 1-Feb-99 | 15-Nov-99 | 3500 | 244 | 16.7 | 0.70 | -4 | 4 | 9 | -2 | 0.751 | 0.1 |
| FBK | SAIN[1] | 1-Feb-99 | 14-Nov-99 | 2044 | 216 | 8.3 | 0.57 | -11 | 11 | 11 | -1 | 0.508 | -2.3 |
| FBK | AROF[1] | 1-Feb-99 | 3-Oct-99 | 4746 | 195 | 44.2 | 0.59 | 0 | 0 | 13 | -1 | 0.783 | -0.8 |
| FBK | ARMI[1] | 1-Feb-99 | 3-Nov-99 | 2862 | 190 | 39.4 | 0.68 | 0 | 0 | 11 | -3 | 0.757 | 0.6 |
| ARG | SAIN | 1-Nov-98 | 14-Nov-99 | 457 | 355 | 25.8 | 0.52 | 10 | 10 | 14 | 6 | 0.307 | 0.5 |
| ARG | SAMI | 1-Nov-98 | 15-Nov-99 | 1488 | 334 | 28.0 | 0.39 | 17 | 17 | 16 | 1 | 0.507 | 0.6 |
| ARG | SAOF | 1-Nov-98 | 15-Nov-99 | 901 | 311 | 39.2 | 0.46 | 19 | 19 | 15 | 2 | 0.711 | -2.4 |
| ARG | AROF | 1-Nov-98 | 3-Oct-99 | 3218 | 220 | 13.4 | 0.60 | 0 | 0 | 12 | 1 | 0.733 | -3.1 |
| ARG | ARMI[1] | 1-Nov-98 | 3-Nov-99 | 2127 | 215 | 7.7 | 0.59 | 0 | 0 | 11 | -1 | 0.642 | -2.1 |
| ARG | SMIN | 1-Nov-98 | 7-Mar-99 | 913 | 137 | 26.7 | 0.62 | -7 | 7 | 19 | -4 | 0.438 | 8.4 |
| PTC | ARMI | 1-Jun-98 | 28-Jan-99 | 2521 | 291 | 22.2 | 0.74 | 9 | 9 | 10 | 2 | 0.786 | -3.7 |
| PTC | AROF | 1-Aug-97 | 3-Oct-99 | 6636 | 279 | 25.2 | 0.58 | 6 | 6 | 14 | 2 | 0.757 | -4.5 |
| PTC | AROF[1] | 1-Jun-98 | 28-Jan-99 | 3717 | 279 | 25.2 | 0.71 | 1 | 1 | 10 | 3 | 0.839 | -4.3 |
| PTC | SMOF[1] | 1-Jun-98 | 28-Jan-99 | 3009 | 177 | 33.0 | 0.63 | -12 | 12 | 9 | -2 | 0.756 | -2.5 |
| PTC | SMIN[1] | 27-Jun-98 | 28-Jan-99 | 2904 | 160 | 5.7 | 0.77 | -16 | 16 | 7 | 1 | 0.845 | -1.2 |
| RFG | ADCP[1] | 20-May-98 | 12-Oct-99 | 10186 | 147 | 28.0 | 0.50 | 1 | 1 | 12 | 4 | 0.736 | -1.9 |
| COP | ADCP[1] | 20-May-98 | 12-Oct-99 | 6659 | 189 | 17.7 | 0.60 | -1 | 1 | 11 | -3 | 0.883 | 3.5 |

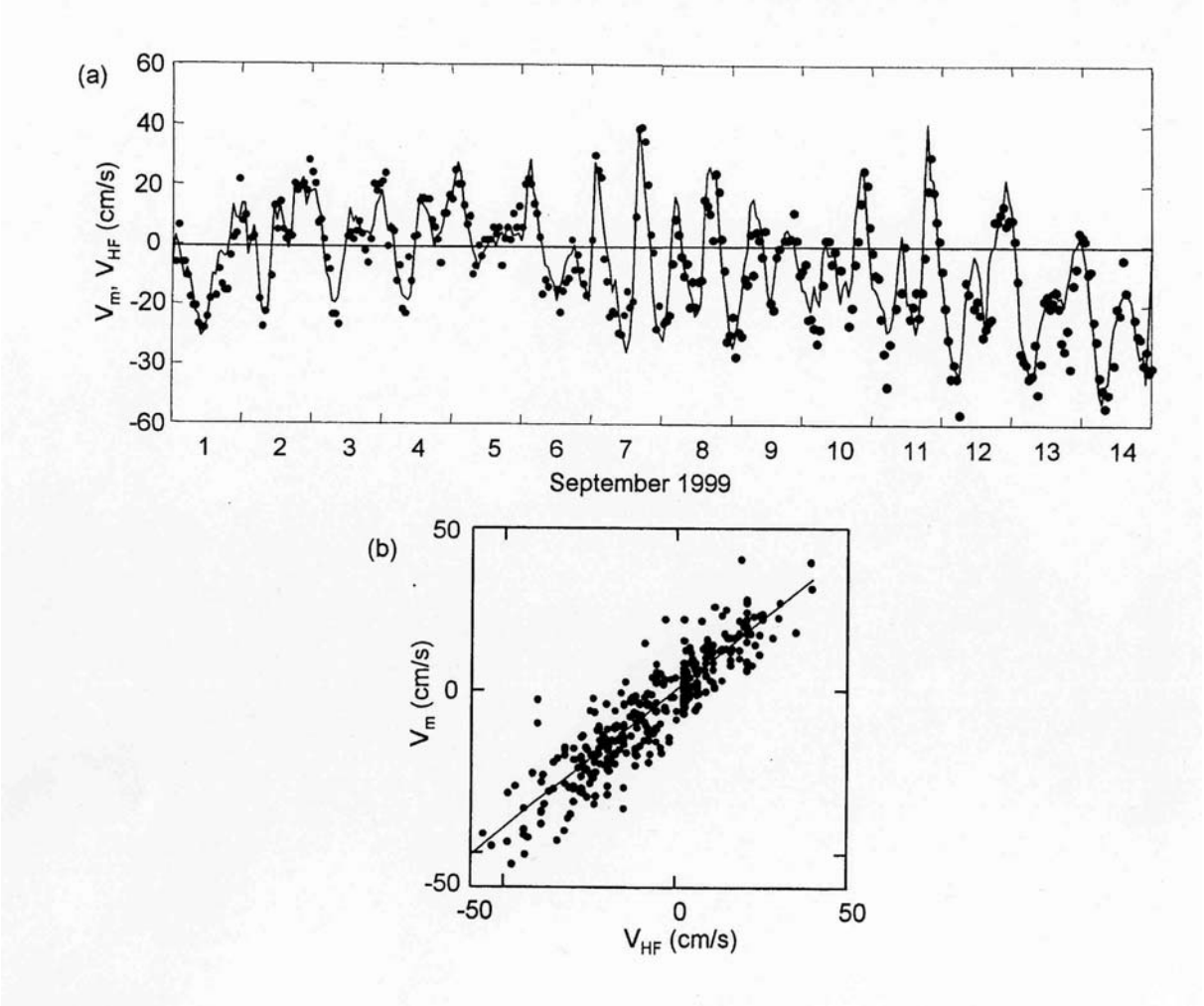


**Figure 3**. **(a)** Time series of radial currents $V_m$ from mooring SAMI (solid line) and radial currents $V_{HF}$ from the FBK radar (dots) for 1-14 September 1999. **(b)** Scatter plot of $V_m$ versus $V_{HF}$ in panel (a). $V_m$ and $V_{HF}$ are significantly correlated with $r^2 = 0.81$, N= 314 and are related such that $V_{HF} = 0.846\ V_m + 0.535$.

Good operating conditions and high signal to noise ratios resulted in low rms radial speed differences (9-13 cm $s^{-1}$) and generally high $r^2$ (0.59 - 0.70) for the FBK radar (Table 1). Comparable rms differences (7-10 cm $s^{-1}$) and $r^2$ (0.63-0.77) were found for the PTC radar for the period 1 June 1998 through 28 January 1999 when unlimited access to the site allowed routine maintenance and repair. Before and after this period, hardware problems reduced the performance of the PTC radar. This is indicated for the PTC-AROF pair by the lower $r^2$ (0.58) and greater rms differences (14 cm $s^{-1}$) for the full time series, 1 August 1997 through 3 October 1999. Similar results were found using the full time series when PTC was paired with the other moorings of Table 1 (results not shown). The greatest rms differences (11-19 cm $s^{-1}$) and lowest $r^2$ (0.39-0.62) were observed between the ARG radar and surrounding moorings due to reduced signal to noise ratios caused by antenna and cable problems.

The longest time series, each with more than 6000 hourly data points, were obtained from the ADCP mooring and the RFG and COP radars. These radars had consistently high signal-to-noise ratios during the mooring deployment period, but with $r^2$ (0.50 - 0.60) and rms differences (12 - 11 cm $s^{-1}$) comparable to the other pairs. This may have resulted from the large watch circle of the ADCP mooring (radius ~750 m); we were unable to account for mooring motions.

### 3.2 Coverage variations

An overall indicator of radar performance is spatial coverage over time. Coverage is defined as the number of sectors returning radials each hour (Figure 2b-f). Some moorings were near the range limits of the radars (42 km) or near the edge of angular coverage range (e.g., ABOF in Figure 1). Angular coverage typically extended to within a few degrees of the surrounding coastline. Consistently high coverage obtained at FBK corresponded to high signal to noise ratios, low rms differences, and high $r^2$. At ARG, low, intermittent coverage during the comparison period corresponded to lower $r^2$ and higher rms differences. An increase in coverage at ARG in November 1999, after the comparison period, resulted from antenna and cable replacement. Causes of coverage variability include power outages, antenna collapse, or other hardware failures. For example, at RFG in April 1998 animals bit partially through the transmit cable, causing poor transmission, lower signal-to-noise ratios, and frequent signal loss. Transmit and receive cables were then enclosed in electrical conduit. Coverage variations may also result from changing noise sources or variations in the environment around the radar antennas.

High frequency coverage variations were apparent in the time series (Figure 2b-f). An expanded view of a 2-week period of the RFG time series shows that these had a strong diurnal component (Fig 4a). Strong diurnal peaks occurred in the spectra of coverage time series from all sites (data not shown). Hourly coverage maps (Figure 4b and 4c) show that the diurnal variation resulted from patchiness in coverage, as well as extensions and contractions of range, as observed by (Paduan and Rosenfeld 1996). For RFG the diurnal coverage reached a maximum around 1400 local time each day and a minimum about 12 hours later (Figure 4a). In addition to diurnal variations, large fluctuations extending over a range of time scales are evident in the coverage record, often obscuring the diurnal pattern.

### 3.3 Spectral analysis

Power spectra of $V_{HF}$ and $V_m$ were computed for subsets of the time series of Figure 2 to compare variance levels over time scales of 2 hours to ~20 days. Subsets were chosen to avoid large data gaps occasionally lasting over a month (Figure 2). For each subset of data, up to 30% of data were missing, and these were filled with zeroes. Representative power spectra for three HF radar-moorings pairs are shown in Figure 5. Spectral levels generally agreed for frequencies less than 2.3 cycles $day^{-1}$ (cpd), but levels of $V_{HF}$ tended to be somewhat less than $V_m$ such as for PTC-SMOF in Figure 5. This is consistent with the observation that regression line slopes were less than 1. The diurnal (K1) and semidiurnal (M2) tidal peaks in $V_m$ and $V_{HF}$ were well resolved for FBK-SAOF and PTC-SMOF, and SMIN, but not for the ARG radar. Shoulders in the FBK-SAOF spectra suggest a poorly resolved peak near the inertial frequency (1.13 cpd). Above ~2.2 cpd $V_{HF}$ spectra become nearly white and depart sharply from $V_m$ spectra. At these frequencies $V_m$ spectra have slopes in the range -3 to -2.

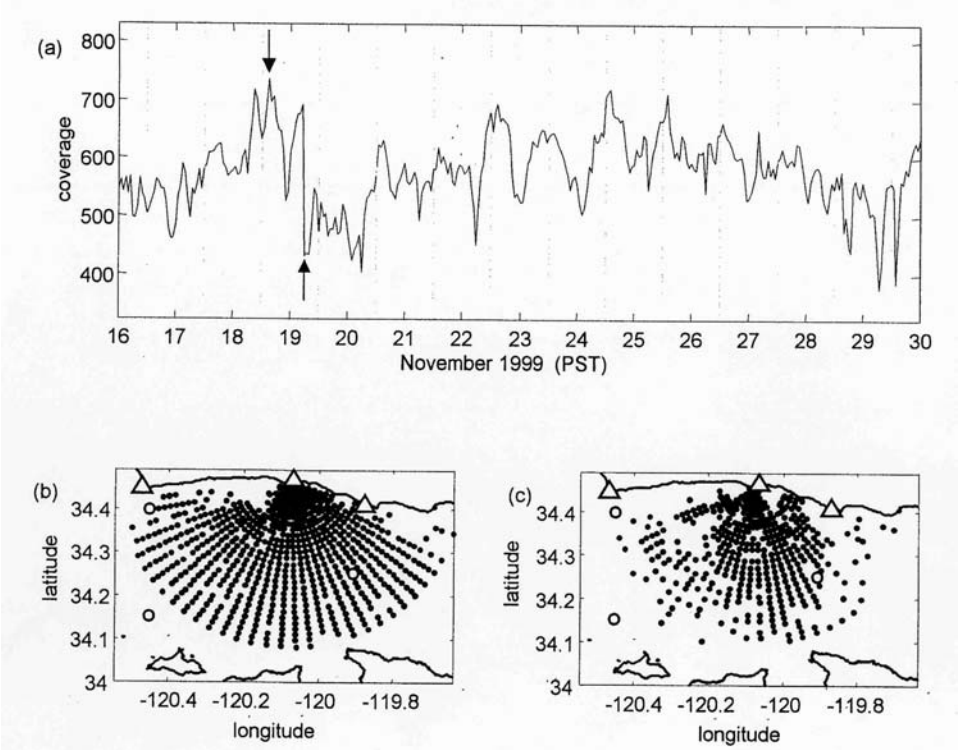


**Figure 4. (a)** Time series of coverage at RFG for 16-30 November 1999 showing strong diurnal variations. Coverage was defined as the number of sectors returning radial currents each hour. Vertical lines indicate local noon. Arrows indicate times of high coverage, shown in **(b)**, and low coverage **(c)**.

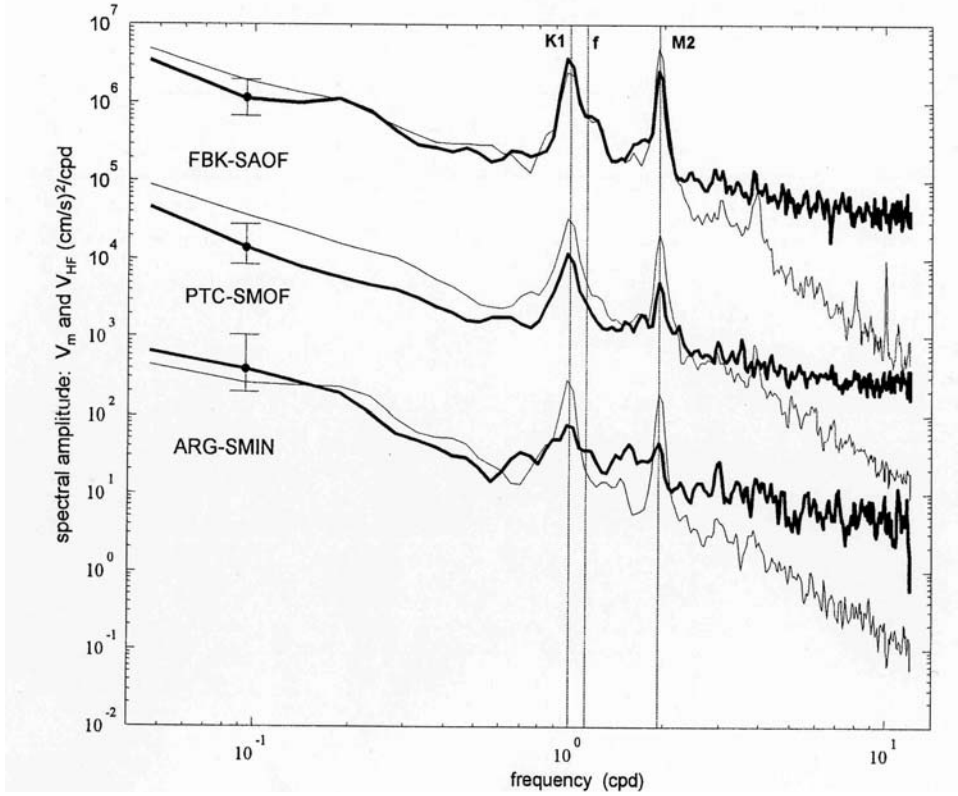


**Figure 5**. Pairs of power spectra of radial vectors from three HF radars (bold lines) and three moorings (light lines). From top to bottom radar-mooring pairs are FBK-SAOF, PTC-SMOF, and ARG-SM1N. Vertical lines denote the K1 and M2 tidal frequencies, and f indicates the inertial frequency. The upper two pairs of spectra are offset vertically by factors of $10^2$ and $10^4$, respectively.

Squared coherence spectra $\gamma^2$ were computed between several time series of $V_{HF}$ and $V_m$ (denoted by superscript 1, column 2 of Table 1) to examine correlation versus frequency; the envelope of these spectra is indicated by shading in Figure 6a. Spectra of $\gamma^2$ were averaged together to produce $\overline{\gamma^2}$ as an overall measure of coherence versus frequency (bold line, Figure 6a). The standard deviation $\sigma$ at each frequency was computed as a measure of variability in $\gamma^2$ (thin solid lines indicate $\overline{\gamma^2} \pm 1\ \sigma$ in Figure 6a). $\overline{\gamma^2}$ fell in the range 0.3-0.7 up to frequencies of about 2.3 cpd where it dropped below the threshold labeled 95%. The threshold was defined such that $\gamma^2$ between two unrelated time series would exceed this level only *5* times out of 100. This result indicates significant coherence between $V_m$ and $V_{HF}$ for frequencies less than ~2.3 cpd, the same frequency range over which their power spectra agree (Figure 6). The phase spectrum was nearly zero over this range and became highly variable at frequencies where $\overline{\gamma^2}$ was not significant (Figure 6b).

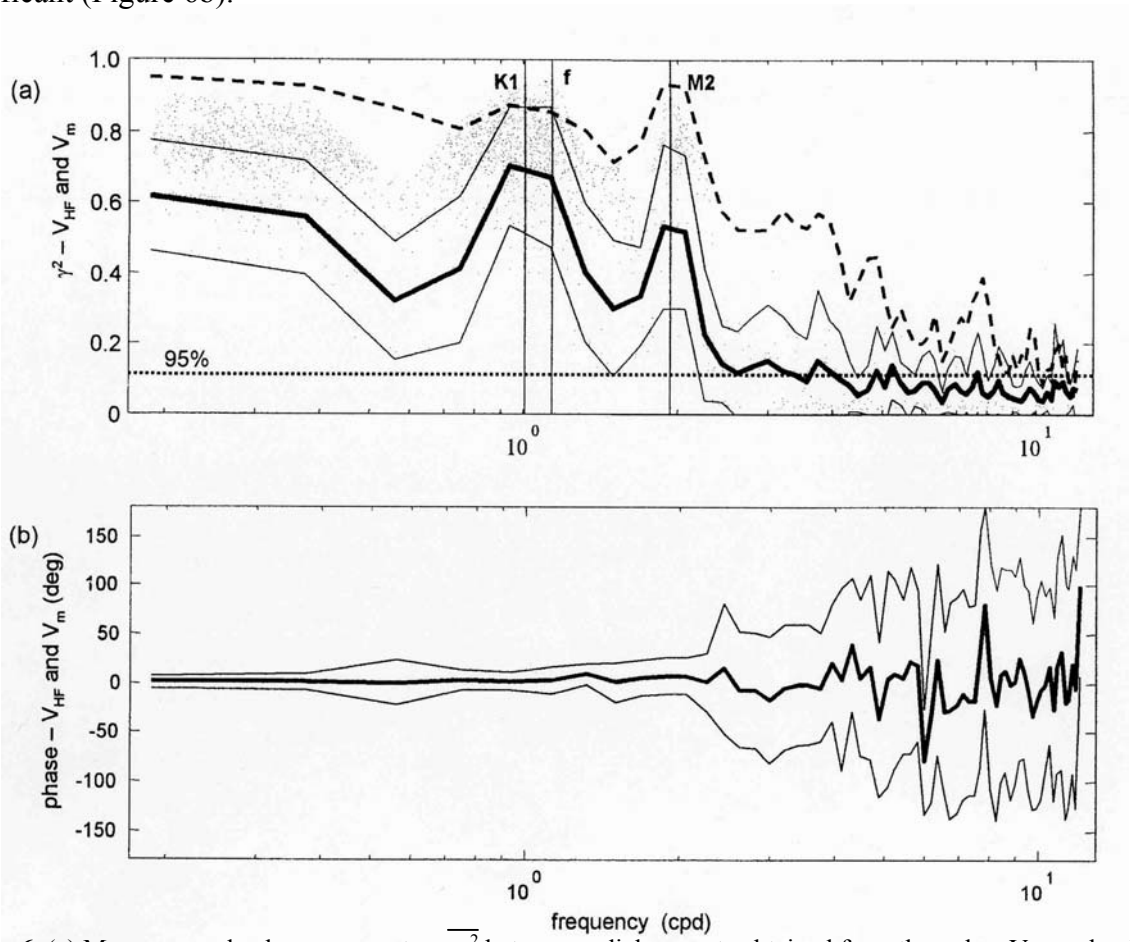


**Figure 6.** (a) Mean squared coherence spectrum $\overline{\gamma^2}$ between radial currents obtained from the radars $V_{HF}$ and radial currents obtained from the moorings $V_m$ (bold line). Time series used in computing $\overline{\gamma^2}$ are indicated in column 2 of Table 1 by superscript 1. $\overline{\gamma^2} \pm 1$ standard deviation are shown (thin lines) along with envelope of all $\gamma^2$ spectra (shading). $\gamma^2$ between radial currents measured by the acoustic Doppler profiler at 3.2 m and 8.2 m depth is also shown (dashed line). Vertical lines denote the K1 and M2 tidal frequencies, and f indicates the inertial frequency. Dotted line shows threshold for significance at 95% confidence. (b) Mean phase spectrum (bold line) ± 1 standard deviation (thin lines) between $V_{HF}$ and $V_m$ corresponding to $\overline{\gamma^2}$ spectrum of panel (a).

To investigate how vertical shear near the surface might the affect coherence between $V_{HF}$ and $V_m$, we computed $\gamma^2$ between ADCP time series at 3.2 m and 8.2 m depths (dashed line, Figure 6a). This depth difference is comparable to the difference in measurement depths of the radars and VMCM's. The rms difference between the ADCP time series at these depths was 5 cm $s^{-1}$ over the 12,048 hr deployment period. The $\gamma^2$ spectrum for the ADCP over this depth range was higher than $\overline{\gamma^2}$ for $\underline{V_m}$ and $V_{HF}$, but had a somewhat similar shape. Around the diurnal peak, levels representing the $\overline{\gamma^2}$ +1 $\sigma$ were comparable to $\gamma^2$ for the ADCP as were some of the individual $\gamma^2$ spectra based on the envelope. At higher frequencies $\gamma^2$ for the ADCP dropped off more slowly.

### 3.4 Bearing offsets

The sector with the highest $r^2$ between $V_{HF}$ and $V_m$ often did not contain the mooring where $V_m$ was measured, but was displaced in bearing. This displacement suggests errors in the radar's determination of direction to sectors on the ocean's surface. A similar result was reported by (Kosro *et al.* 1997) from an OSCR system. We argue that in the absence of directional errors, the highest $r^2$ will coincide with the sector containing the mooring. A broad peak in $r^2$ may occur if the spatial correlation scales of the velocity field are large in the azimuthal and radial directions. We define the displacement in bearing, or bearing offset $\Delta\theta$, as,

$$\Delta\theta = \theta_r - \theta_m, \qquad (2)$$

where $\theta_r$ is the bearing to center of the sector with maximum $r^2$ and $\theta_m$ is the bearing to the mooring. Positive $\Delta\theta$ indicates that the sector with maximum $r^2$ is displaced clockwise from the mooring. Column 9 of Table 1 shows $\Delta\theta$ for each of the 18 HF radar-mooring pairs. $\Delta\theta$ ranged from -16° to 19° with an average absolute value of 7°, although $\Delta\theta$ could only be determined to within the 5° sector width.

An example of a large bearing offset, $\Delta\theta$ = -16°, was found for PTC-SMIN (Figure 7a). The maximum in $r^2$ was broad, but its peak was clearly offset from SMIN as indicated by $r^2$ profiles along constant range lines of 4.5, 6.0, and 7.5 km (Figures 7b, 7c, and 7d, respectively). The maximum $r^2$ occurred in the same 1.5 km range cell as SMIN, such that the offset was in bearing only. A small bearing offset was found for COP-ADCP with $\Delta\theta$ = -1°. Here the sector with maximum $r^2$ contained the mooring location (Figure 8a) and a broad maximum extended over bearing and range (Figures 8a, 8b, and 8c). Figure 9 shows how $\Delta\theta$ changed with bearing for the PTC, ARG, and FBK radars, which all had more than one mooring within their coverage areas. At PTC, with four moorings in its coverage area, $\Delta\theta$ increased roughly monotonically with bearing from $\Delta\theta$ = -15° at bearing 160° to $\Delta\theta$ = 9° at 291° (open squares, Figure 9). Values of $\Delta\theta$ were only determined near the end points of this range, however. At ARG, $\Delta\theta$ also increased with bearing up to a maximum of $\Delta\theta$ = 19° at 311° followed by a decrease to $\Delta\theta$ = 10° at 355°. At FBK, $\Delta\theta$ reached a minimum of -11° at 216° then increased to 16° at 299°.

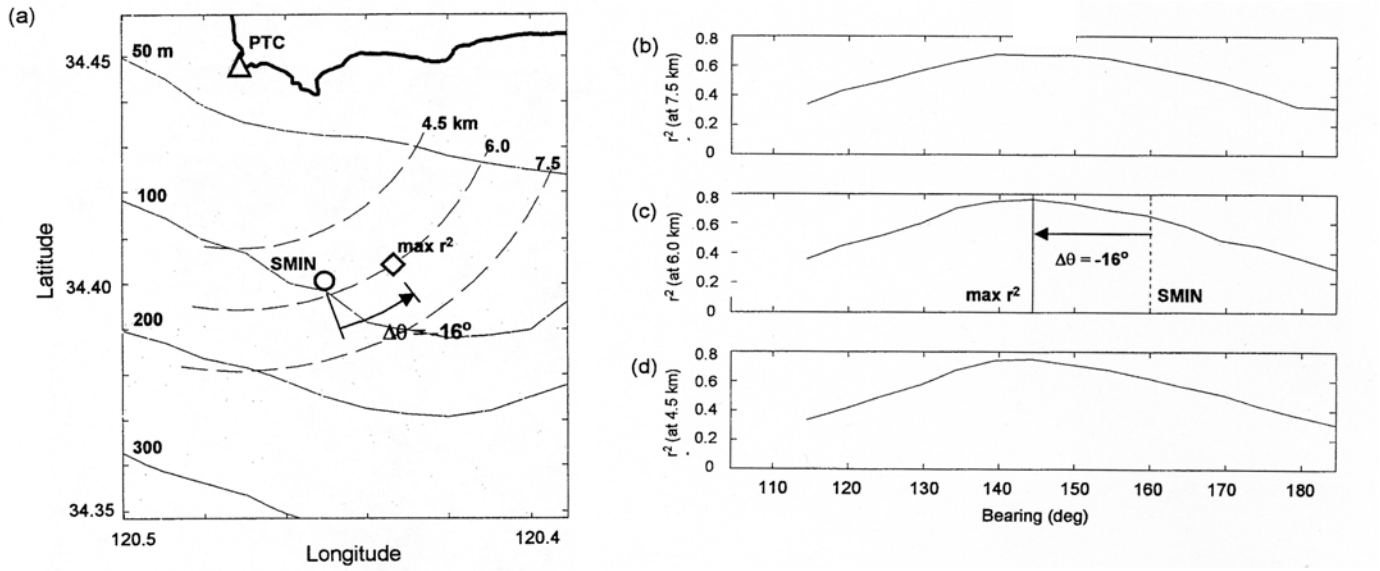


**Figure 7. (a)** Location of Point Conception radar PTC (triangle) and mooring SMIN (circle). Radial current vectors $V_{HF}$ were found for sectors 1.5 km in radius by 5° in azimuth (gray lines). Radial currents $V_m$ were measured *in situ* at the mooring. The diamond indicates the sector with the highest $r^2$ between $V_{HF}$ and $V_m$. The arrow shows bearing offset $\Delta\theta$ between the mooring location and the sector with highest $r^2$. Dashed arcs show the locations of $r^2$ profiles plotted in panels **(b)**, **(c)**, and **(d)**. Profile of $r^2$ between $V_{HF}$ and $V_m$ along ranges of (b) 4.5 km, (c) 6.0 km, and (d) 7.5 km.

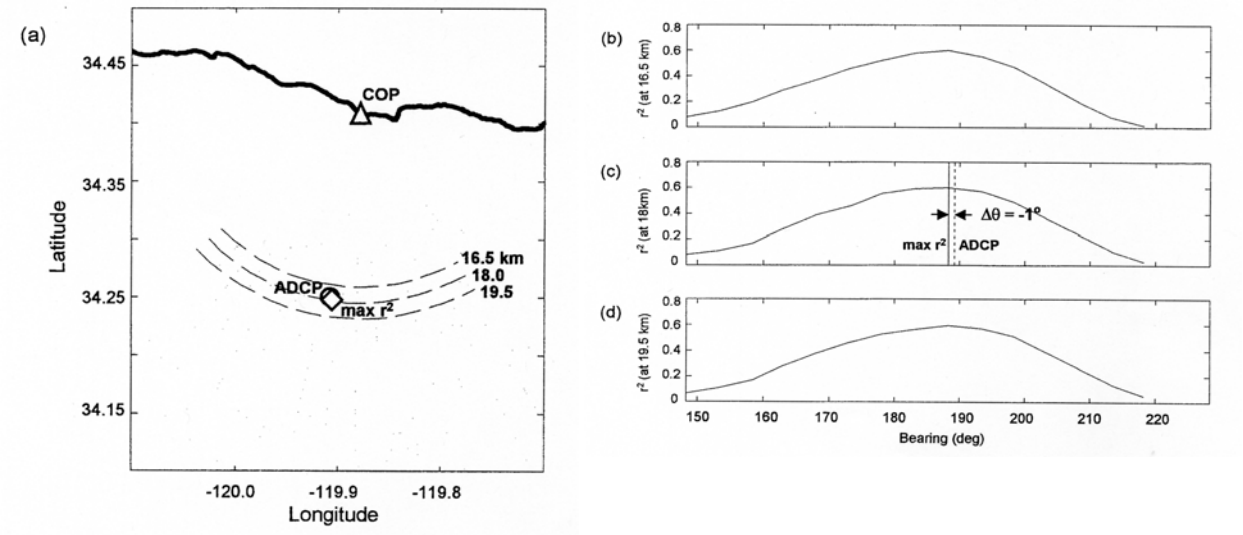


**Figure 8. (a)** As in Figure 7, but for the Coal Oil Point radar COP and mooring ADCP. Profiles of $r^2$ between $V_{HF}$ and $V_m$ along ranges of **(b)** 16.5 km, **(c)** 18.0 km, and **(d)** 19.5 km.

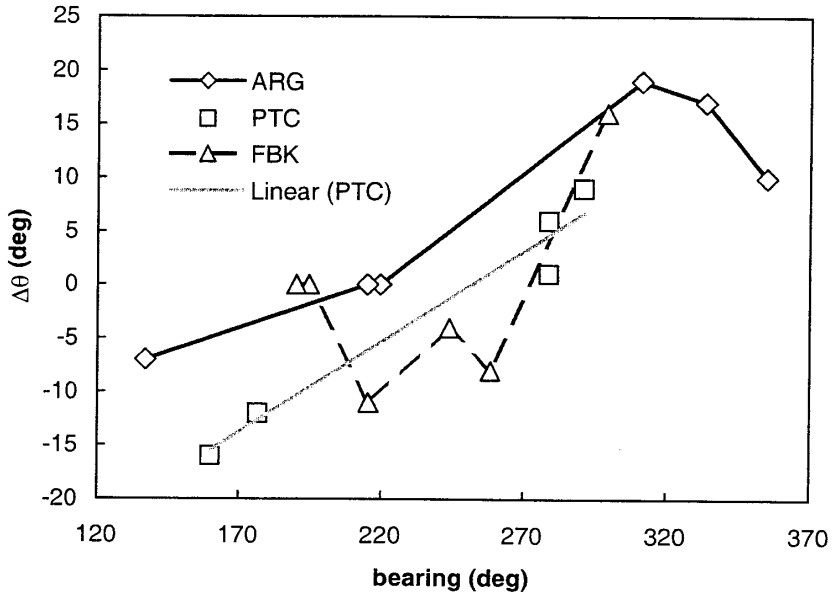


**Figure 9.** Bearing offset Δθ versus bearing for all radars with more than one mooring in coverage areas: Point Conception (PTC, squares, gray line is a linear least square fit), Point Arguello (ARG, diamonds, solid black line), and Fallback-22 (FBK, triangles, dashed line).

## 4. Discussion

An operational characteristic of surface current measuring HF radars is variability in range and azimuthal coverage. (Paduan and Rosenfeld 1996) suggest this results from range variations and failure of the direction finding algorithm to differentiate radial currents as a function of bearing within range cells. We found changes in range and azimuthal coverage spanned a range of time scales, but a diurnal variation was prominent, consistent with results of (Prandle *et al.* 1993) and (Paduan and Rosenfeld 1996). Changes in sea state and variability in the distribution of the waves producing Bragg scattering from the sea surface may be responsible. Coverage variability may also result from changes in the environment around the antennas, such as daily variations in moisture content in surrounding soils and vegetation, or changes in the atmosphere as suggested by (Prandle *et al*. 1993). Additionally, it is well known that the ionosphere's lowest layer, the D-region, has a diurnal cycle. The D-region nearly disappears at night, allowing HF radio waves to travel over long distances (~$10^3$ to $l0^4$ kin) by reflecting off higher ionospheric layers (e.g., Davies 1990). HF transmissions from great distances can become external noise to HF radars, leading to lower signal-to-noise ratios and poor coverage. As an example, an investigation of unusually strong diurnal coverage variations, and poor signal-to-noise ratios, at the PTC radar revealed media broadcasts as the cause.

The rms differences we observe between radial velocity components $V_{HF}$ and $V_m$ (Table 1) are comparable in range (7 - 19 cm $s^{-1}$) and mean (12 cm $s^{-1}$) to rms differences in total velocity components reported elsewhere. (Shay *et al*. 1995) reported rms differences of 11 - 15 cm $s^{-1}$ between OSCR observations and *in situ* current meters off the North Carolina coast. (Shay *et al*. 1998) found somewhat larger rms differences, 18-19 cm $s^{-1}$ on the inshore boundary of the Florida Current using 05CR, although the depth difference between the HF radar and current meter depths was 15 m. (Paduan and Rosenfeld 1996) reported rms differences of 6.2 and 10.8 cm $s^{-1}$ around Monterey Bay using CODAR systems and a moored ADCP. Graber *et al*. (1997)

compared OSCR with several current meters moored in the depth range 5-30 m and report rms differences in the range 10-20 cm $s^{-1}$.

The weak trend of increasing rms differences between $V_{HF}$ and $V_m$ with increasing range (Table 1) is consistent with the effects of horizontal variability in the velocity field. When data from ARG were not included, rms differences were correlated with range ($r^2$ =0.32, N = 16). As discussed by (Graber *et al*. 1997), differences in spatial sampling between current meters and HF radars can produce measurement differences. The VMCM's sample at points around mooring watch circles and HF radars sample sectors of varying size, depending on range. For our radar sites, sectors containing moorings had widths from 0.5 km to 3.9 km corresponding to ranges of 5.7 to 44 km (Table 1, Figure 1). Assuming the moorings were up to ½ the sector width or length (1.5 km) away from the moorings, the moorings and points within sectors could have been as much as ~2 km apart. Effective separations could have been larger if, for example, an average hourly radial were dominated by individual radial estimates from a sector edge and the mooring were at an opposite edge of the sector. Figure 10 of (Graber *et al*. 1997) shows an expected rms difference derived from OSCR total velocity data of about 5-6 cm $s^{-1}$ resulting solely from a horizontal separation of 2 km between measurements. Kosro (1987) computed the structure function of horizontal velocity differences using shipboard ADCP data in an upwelling regime to find expected difference of 7 cm $s^{-1}$ for a 2 km separation.

Vertical separation of HF radar and mooring measurements may have also contributed to differences between $V_{HF}$ and $V_m$. The 5 cm $s^{-1}$ rms difference between the 3 m and 8 m bins at the ADCP mooring is likely a lower limit for typical near-surface vertical current shear in the radar coverage area. The ADCP was moored in an area of lower winds in the Santa Barbara Channel compared with winds at the VMCM moorings. Dorman and Winant (2000) show the highest annual average winds occur in the western portion of our coverage area, in the vicinity of Pt. Conception and Pt. Arguello. Assuming that vertical current shear is primarily wind driven, the 5 cm $s^{-1}$ rms difference we measured probably represents a lower bound on the difference between the surface and 5 m measurements.

Limited resolution of the HF radar's Doppler spectra also contributes to rms differences between $V_{HF}$ and $V_m$. The length of the time series used to compute the Doppler spectrum (256 s for these data) sets the radar's spectral resolution (Barrick 1980). This effectively limits the resolution of $V_{HF}$ to discrete levels separated by $\Delta V_{HF}$ = 4.3 cm $s^{-1}$. The conversion of continuously valued currents into discrete levels produces rms errors of $(1/12)^{1/2} \bullet \Delta V_{HF}$ = 1.2 cm $s^{-1}$ [Bendat J.S., 2000 #64]. It also produces uncertainty in spectral levels (figure *5)* corresponding to 0.13 $cm^2 s^{-2}$ $(cpd)^{-1}$.

The small effect of the limited Doppler spectral resolution, along with the significant effect of horizontal and vertical separation, may account for a significant portion of the observed rms differences. Assuming errors of 5-6 cm $s^{-1}$ due to near surface vertical shear, and 5-7 cm $s^{-1}$ due to horizontal velocity differences, about 50% of the typical rms difference (~12 cm $s^{-1}$) between $V_{HF}$ and $V_m$ could be explained by the different sampling techniques of the radars and current meters.

The bearing offset $\Delta\theta$ may result from several causes. Easily dismissed explanations include misalignment of the receive antenna, and compass errors in the mooring current meters. The HF radar receive antennas were carefully oriented in bearing through a calibration procedure. Repeated checks indicated antenna alignments are constant in time to within ~l°. Misalignment

of the receive antenna would result in constant $\Delta\theta$ at each of the moorings around a given radar. Figure 9 shows that this is not the case: $\Delta\theta$ varies in magnitude and sign for each mooring-radar pair. Similarly, current meter compass error cannot explain the variation of $\Delta\theta$ with bearing. If compass error alone accounted for $\Delta\theta$, then pairs using the same VMCM would show similar $\Delta\theta$. Table 1 shows this is not true: for example, for the FBK-SAOF pair $\Delta\theta = -8°$, but for ARG-SAOF $\Delta\theta = 19°$.

A more likely explanation of $\Delta\theta$ is given by (Barrick and Lipa 1986), who examined the influence of antenna patterns on radial currents. Antenna patterns describe the directional response of the receive antenna to incoming HF radiation. Ideally, only the antenna's design determines the antenna pattern. However, the patterns are also affected by conductors located within about one wavelength of the antenna (~25 m), referred to as the near field. These conductors couple with the antenna, distort the antenna pattern, and produce errors in bearing. For example, (Barrick and Lipa 1986) found severely distorted antenna patterns during a deployment on an offshore oil platform, with rms bearing offsets ~35°. We measured antenna patterns at PTC, RFG, and COP by moving a transponder in a small boat along circular arcs within the coverage areas of the radars. Antenna patterns from these sites exhibited varying levels of distortion (data not shown). Antenna patterns measured at REG and PTC were typical of patterns found elsewhere, while patterns at COP were moderately distorted (D. Barrick, personal communication, 1999).

In principle, antenna pattern distortions can be accounted for in the MUSIC algorithm, and techniques for doing so are in development (e.g., Barrick and Lipa 1999). During the data collection phase of this study, corrections for antenna pattern distortion were unavailable, and HF data used to compute $\Delta\theta$ assumed ideal antenna patterns. We compared observations of $\Delta\theta$ with measured antenna patterns to look for a direct relationship between distortions in the measured patterns and non-zero values of $\Delta\theta$. For example, following a suggestion by J. Paduan (personal communication, 2000), a relationship between $\Delta\theta$ and the rate of change of the measured antenna responses versus bearing was investigated. Extensive experimentation failed to reveal a consistent relationship between $\Delta\theta$ and measured antenna patterns. When procedures for incorporating measured antenna patterns into estimates of $V_{HF}$ are available, we intend to test them by mapping $r^2$ around moorings as in figures 7 and 8. We hypothesize that accounting for antenna pattern distortions would result in lower $\Delta\theta$.

Another factor affecting $\Delta\theta$ is phase calibration of the three-element receive antenna. Each element responds to incoming signals with differing voltage phases. Phases were initially determined at PTC from sea echo as part of the CODAR data processing procedures (Barrick and Lipa 1986). Later, phases were directly measured with the transponder during the antenna pattern measurements and used in processing. We computed $\Delta\theta$ between PTC and SMIN for each of these time periods to test the effect of phase settings. Using sea echo phases resulted in $\Delta\theta$ $\sim=30°$, while transponder phases resulted in $\Delta\theta$ ,$\sim=15°$. The reduction in $\Delta\theta$ using the transponder phase suggests a strong link between receive antenna characteristics and $\Delta\theta$.

Bearing offsets $\Delta\theta$ in HF radial data ultimately produce errors in total velocity vectors determined from two or more radars. We examined effects of variable $\Delta\theta$ on total velocity vectors by simulating its effect on an idealized flow field. For simplicity, we used a uniform westward flow along a straight coast (gray arrows, Figure 10). Patterns of $V_{HF}$ as functions of range and bearing were computed at two sites labeled A and B in Figure 10. At site A, bearings

to sectors on the sea surface were distorted by Δθ using the slope of the linear least square fit for the PTC radar (gray straight line, Figure 9): over bearings 90° - 270°, Δθ in the range -l8° to 14° were added to the bearing. Total velocity vectors (black arrows, Figure 10) were computed on a 2 km grid, from $V_{HF}$ at sites A and B. Following the method of (Gurgel 1994), a total velocity vector at each grid point was computed from all $V_{HF}$ within a circle (3 km radius) centered on the grid point. A similar procedure was used by Paduan and Rosenfeld (1996). The mean difference in flow speeds between the original vectors (gray arrows, Figure 10) and distorted vectors (black arrows, Figure 10) was ~7% of the original uniform flow speed with a maximum difference of ~15%. The mean difference in flow direction was ~2.5°, with a maximum of ~9°. Simulations with other simple flow fields produced comparable errors in total velocities (results not shown). These errors are significant and reinforce the need for incorporation of antenna pattern corrections in the direction finding algorithms used with these radar systems.

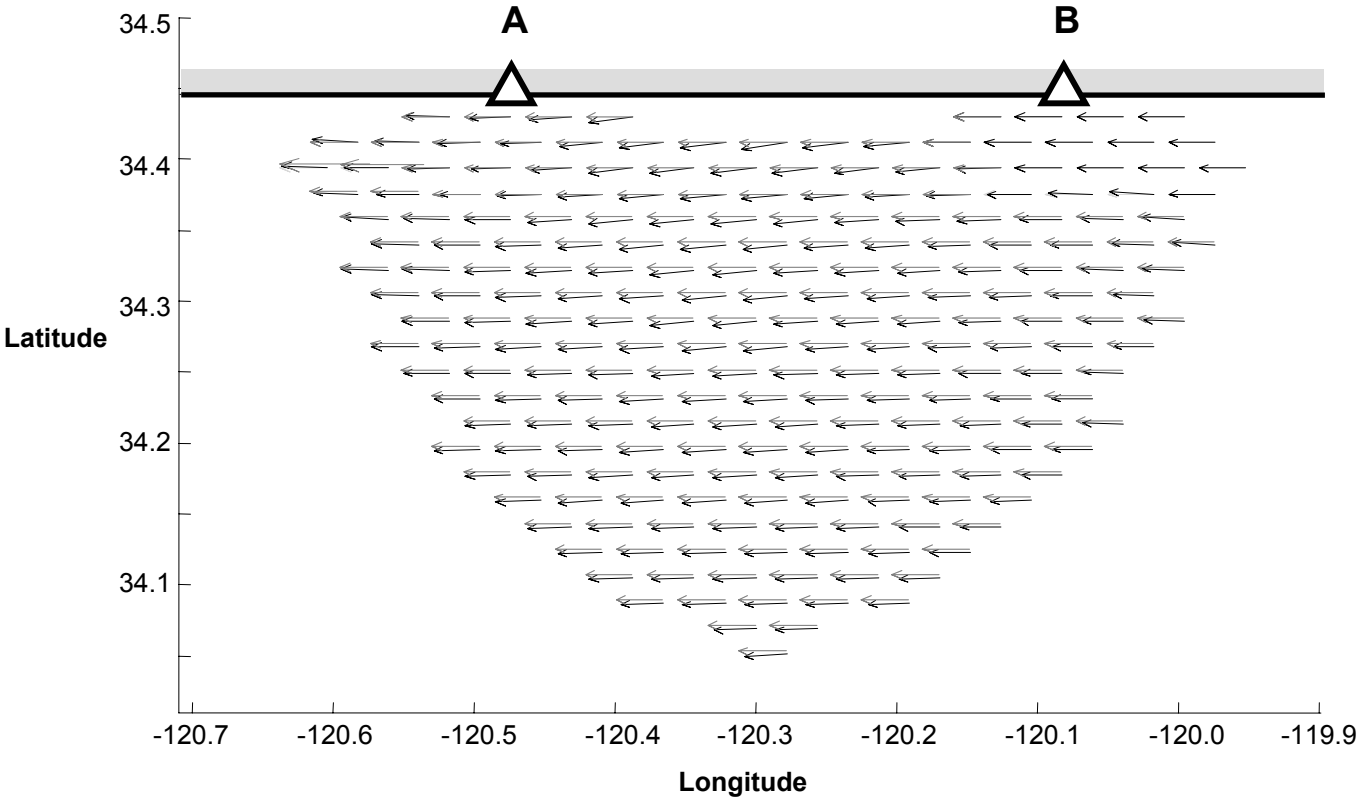


**Figure 10.** Gray arrows (offset for clarity) show uniform westward flow parallel to a straight coastline (bold line and shading) used for modeling effects of bearing offset Δθ on total velocity vectors. Arrows were placed on grid with 2 km spacing. Black arrows show total vectors computed from radar sites located at A and B (triangles). Radial currents $V_{HF}$ measured at A were distorted by bearing offset Δθ as explained in text.

## 5. Conclusions

We compared radial components of near-surface ocean currents (radials) from 18 pairs of moored current meters and five HF radars (transmitting at frequencies of 12-13 Mhz) from the Santa Barbara Channel and Santa Maria Basins. Comparisons were based on observations between June 1997 and November 1999 with record lengths of 5 to 424 days. Eight vector measuring current meters moored at 5 m depth and one acoustic Doppler current profiler with its shallowest bin at 3.2 m were compared with HF radar currents at ~1 m. Our analysis supports the following conclusions:

1. Radials obtained from the radars were significantly correlated with radials obtained from the moored current meters with $r^2$ in the range 0.39-0.77. Root-mean-square (rms) radial speed differences ranged from 7-19 cm $s^{-1}$. A weak trend of increasing rms differences was found with increasing range.
2. Significant coherence was found between current meter and radar-derived time series for frequencies below 2.2 cpd (11 hour period and longer). Power spectra show similar magnitudes and slopes for frequencies below 2.2 cpd.
3. A pointing error $\Delta\theta$ ranging from -l6° to19° was found for some of the radar sites where positive values indicate a clockwise error. $\Delta\theta$ for a given radar was not constant, but varied with bearing. We speculate that $\Delta\theta$ resulted from distortions of the receive antenna patterns in the near field.
4. We used a simple model of $\Delta\theta$ versus bearing based on our observations to simulate errors in total velocity vectors computed from two radars. Using a uniform flow parallel to shore, $\Delta\theta$ produced speed errors of up 15% and direction errors up to 9° in total velocity vectors.

**REFERENCES**

Barrick, D.E. 1980: Accuracy of parameter extraction from sample-averaged sea-echo Doppler spectra. *IEEE Transactions on Antennas and Propagation,* **28**(1): 1-11.

Barrick, D.E., and B.J. Lipa, 1986: Correcting for Distorted Antenna Patterns in CODAR Ocean Surface Measurements. *IEEE Journal of Oceanic Engineering,* **OE—11** (2): 304-309.

Barrick, D.E., and B.J. Lipa, 1997: Evolution of bearing determination in HF current mapping radars. *Oceanography,* **10** (2): 72-75.

Barrick, D.E., and B.J. Lipa, 1999: Using antenna patterns to improve the quality of SeaSonde HF radar surface current maps. *IEEE 6th Working Conference on Current Measurement.*

Chapman, R.D., and H.C. Graber, 1997: Validation of HF radar measurements. *Oceanography,* **10** (2): 76-79.

Chapman, R.D., L.K. Shay, H.C. Graber, J.B. Edson, A. Karachintsev, C.L. Trump, and D.B. Ross, 1997: On the accuracy of HF radar surface current measurements: Intercomparison with ship-based sensors. *Journal of Geophysical Research,* **102** (C8): 18,737-18,748.

Crombie, D.D., 1955: Doppler Spectrum of Sea Echo at 13.56 Mc/s. *Nature,* **175**: 681-682.

Davies, K., 1990: Ionospheric Radio. *IEEE Electromagnetic Waves Series,* **31**.

Dorman, C.E., and C.D. Winant, 2000: The Structure and Variability of the Marine Atmosphere around the Santa Barbara Channel. *Monthly Weather Review,* **128**: 261-282.

Georges, T.M., 1980: Progress toward a practical skywave sea-state radar. *IEEE Trans. Antennas Propagat.,* **28** (6): 751-761.

Graber, H.C., B.K. Haus, RD. Chapman, and L.K. Shay, 1997: HF radar comparison with moored estimates of current speed and direction: Expected differences and implications. *Journal of Geophysical Research,* **102** (C8): 18,749-18,766.

Gurgel, K.W., 1994: Shipborne measurement of surface current fields by HF radar. *L 'Onde Elect rique,* **74** (5)*:* 54-59.

Harlan, J.A., S.E. Swearer, R.R. Leben, and C.A. Fox: Surface Circulation in a Caribbean Island Wake. *(in review).*

Harms, S., and C.D. Winant, 1998: Characteristic patterns of the circulation in the Santa Barbara Channel. *Journal of Geophysical Research,* **103** (C2): 3041-3065.

Kosro, P.M., 1987: Structure of the coastal current field off northern California during the coastal ocean dynamics experiment. *Journal of Geophysical research,* **92** (c2): 1637-1654.

Kosro, P.M., J.A. Barth, and T.P. Strub, 1997: The coastal jet: Observations of surface currents over the Oregon continental shelf from HF radar. *Oceanography,* **10** (2): 53-57.

Kraus, J.D., *Antennas,* McGraw-Hill, 1988.

Laws, K.E., D.M. Fernandez, and J.D. Paduan, 2000: Simulation-based evaluations of HF radar ocean current algorithms. *IEEE Journal of Oceanic Engineering,* **25** (4): 481-491.

Melton, D.C., 1995: Remote sensing and validation of surface currents from HF radar. *MS. Thesis, Naval Postgraduate School*, 66pp.

Paduan, J.D., and L.K. Rosenfeld, 1996: Remotely sensed surface currents in Monterey Bay from shore-based HF radar (Coastal Ocean Dynamics Application Radar). *Journal of Geophysical Research,* **101** (C9): 20,669-20,686.

Prandle, D., S.G. Loch, and R. Player, 1993: Tidal flows through the Straits of Dover. *Journal of Physical Oceanography,* **23**: 23-37.

Schmidt, R.O., 1986: Multiple Emitter Location and Signal Parameter Estimation. *IEEE Transactions on antennas and propagation,* **AP-34** (3): 276-280.

Shay, L.K., H.C. Graber, D.B. Ross, and R.D. Chapman, 1995: Mesoscale ocean surface current structure detected by high-frequency radar. *Journal of Atmospheric and Oceanic Technology,* **12**: 88 1-900.

Shay, L.K., S.J. Lentz, H.C. Graber, and B.K. Haus, 1998: Current structure variations detected by high-frequency radar and vector-measuring current meters. *Journal of Atmospheric and Oceanic Technology,* **15**: 237-256.

Stewart, R.H., and J.W. Joy, 1974: HF radio measurements of surface currents. *Deep Sea Research,* **21**: 1039-1049.

Vesecky, J., C. Teague, D. Fernandez, J. Paduan, J. Daida, R. Onstott, K. Laws, and P. Hansen, 1998: Coastal Currents with HF radar. *Backscatter,* **13**: 12-20.

Weller, RA., and R.E. Davis, 1980: A vector measuring current meter. *Deep-Sea Research,* **27**: 565-582.

## The Department of the Interior Mission

As the Nation's principal conservation agency, the Department of the Interior has responsibility for most of our nationally owned public lands and natural resources. This includes fostering sound use of our land and water resources; protecting our fish, wildlife, and biological diversity; preserving the environmental and cultural values of our national parks and historical places; and providing for the enjoyment of life through outdoor recreation. The Department assesses our energy and mineral resources and works to ensure that their development is in the best interests of all our people by encouraging stewardship and citizen participation in their care. The Department also has a major responsibility for American Indian reservation communities and for people who live in island territories under U.S. administration.

## The Minerals Management Service Mission

As a bureau of the Department of the Interior, the Minerals Management Service's (MMS) primary responsibilities are to manage the mineral resources located on the Nation's Outer Continental Shelf (OCS), collect revenue from the Federal OCS and onshore Federal and Indian lands, and distribute those revenues.

Moreover, in working to meet its responsibilities, the **Offshore Minerals Management Program** administers the OCS competitive leasing program and oversees the safe and environmentally sound exploration and production of our Nation's offshore natural gas, oil and other mineral resources. The MMS **Royalty Management Program** meets its responsibilities by ensuring the efficient, timely and accurate collection and disbursement of revenue from mineral leasing and production due to Indian tribes and allottees, States and the U.S. Treasury.

The MMS strives to fulfill its responsibilities through the general guiding principles of: (1) being responsive to the public's concerns and interests by maintaining a dialogue with all potentially affected parties and (2) carrying out its programs with an emphasis on working to enhance the quality of life for all Americans by lending MMS assistance and expertise to economic development and environmental protection.